

Localisation of Fluorescent Probes and the Estimation of Lipid Nanodomain Sizes by Modern Fluorescence Techniques

Radek Šachl

Supervised by Lennart B.-Å. Johansson and Martin Hof

Department of Chemistry: Biological Chemistry
Umeå University, Umeå, SE



Charles University in Prague, Faculty of Science
Department of Physical and Macromolecular Chemistry
Prague, CZ



2012

Copyright © by Radek Šachl, 2012

ISBN: 978-91-7459-390-7

Electronical version accessible on <http://umu.diva-portal.org>

Printed by: VMC-KBC, Umeå University

Umeå, Sweden 2012

Organizations

Umeå University
Department of Chemistry, Umeå, SE
&
Charles University in Prague,
Faculty of Science, Prague, CZ

Document name

Doctoral thesis

Date of issue

February 2012

Author

Radek Šachl

Title

Localisation of Fluorescent Probes and the Estimation of Lipid Nanodomain Sizes by Modern Fluorescence Techniques

Abstract

The thesis is divided into two major parts. The first part focuses on the localisation of probes in lipid/polymeric bilayers and in G_{M1} micelles. Included in this thesis is a new approach based on electronic energy transfer/migration (FRET/DDEM), which efficiently determines transversal positions of fluorescent molecules in lipid bilayers. This approach has been used to locate newly synthesized lipid probes in DOPC bilayers. The label was introduced at the end of *sn*-2 acyl chains of variable length.

Analytical models accounting for FRET exist for a limited number of basic geometries. Here, a combination of FRET and Monte Carlo simulations enables the localisation of probes in bicelles and in bilayers containing pores, *i.e.* in lipid systems with variable curvature, or in non-homogenous lipid systems. This approach has been used to test whether conical-like fluorescence probes have an increased affinity to highly curved regions, which would enable preferential labelling of membrane pores.

A simplified FRET model has been applied to localize 2-pyridones, a class of potential drugs, in G_{M1} micelles. Since the localisation of drugs within nanoparticles might influence the release kinetics and loading efficiency, knowledge about the drug location is highly relevant. It turned out that all derivatives were localised at the core-shell interface of G_{M1} micelles.

The second part of the thesis focuses mainly on the estimation of lipid nanodomain size by means of FRET, which still remains the most powerful method in this field. Limitations of FRET in the determination of domain size have been explored. We showed that the limitations of FRET are mainly caused by a low probes affinity to either the liquid-ordered or liquid-disordered phase. In the continuing work we provided a detailed dynamic and structural study of crosslinker-triggered formation of nanodomains. Here, two different domains have been revealed, *i.e.* *i*) domains whose size grows with increasing amount of added cholera toxin (CTxB), and to which CTxB binds tightly; *ii*) domains formed in membranes containing a slightly increased amount of sphingomyelin (as compared to *i*) whose size does not change during titration by additional CTxB and to which CTxB binds less tightly.

Keywords

Electronic energy transfer/migration, FRET, FCS, Monte Carlo simulations, fluorescence, solvent relaxation, lipid bilayer, rafts, micelles, BODIPY, phase diagram.

Language: English

ISBN: 978-91-7459-390-7

Number of pages: 46 + 7 papers

Organizace
Umeå University
Department of Chemistry, Umeå, SE
&
Univerzita Karlova,
Přírodovědecká fakulta, Praha, CZ

Typ dokumentu
Disertační práce

Datum vydání
únor 2012

Autor
Radek Šachl

Název práce
Lokalizace fluorescenčních značek a určování velikostí lipidových nanodomén pomocí moderních fluorescenčních metod

Abstrakt

Disertace je rozdělena do dvou hlavních částí. První část se zabývá lokalizací značek v lipidových/polymerních dvojvrstvách a v G_{M1} micelách. V práci prezentujeme nový přístup založený na přenosu/migraci elektronické energie (FRET/DDEM), jež umožňuje efektivně určovat vertikální pozici fluorescenčních molekul uvnitř lipidové dvojvrstvy. Tato metoda byla použita k lokalizaci nově syntetizovaných lipidových značek značených na konci *sn*-2 acylového řetězce s různou délkou v DOPC dvojvrstvách.

Analytické modely popisující FRET existují pouze pro limitovaný počet základních geometrií. Kombinace FRETu s Monte Carlo simulacemi nicméně umožňuje lokalizaci značek v bicelách a v dvojvrstvách obsahujících póry, tj. v lipidových systémech s proměnlivým zakřivením a v nehomogenních lipidových útvarech. Tento přístup umožnil např. zjistit, zda kuželovitě tvarované značky mají zvýšenou afinitu k vysoce zakřiveným oblastem dvojvrstvy, což by umožnilo preferenční značení pórů.

Lokalizovány byly rovněž tři deriváty 2-pyridonů (potencionálních léčiv) v G_{M1} micelách za použití jednoduchého modelu zohledňujícího FRET mezi donory a akceptory nacházejícími se v micelách. Lokalizace léčiv v nanočásticích ovlivňuje kinetiku uvolňování (release kinetics) a množství látky solubilizované v micelách (loading efficiency).

Druhá část se především zabývá určováním velikostí lipidových nanodomén pomocí FRETu, který stále zůstává nejvíce výkonnou metodou v této oblasti. Zkoumány byly limitace FRETu v určování lipidových nanodomén. Ukázalo se, že tato omezení jsou především způsobena nízkou afinitou značek buď k L_o nebo k L_d fázi. V navazující studii jsme poskytnuli detailní dynamickou a strukturní studii formace nanodomén indukované crosslinkerem. Objevili jsme dva typy domén: a) domény, jejichž velikost se zvětšuje s rostoucím množstvím přidaného cholera toxinu (CTxB) a k nimž se CTxB váže pevně a b) domény vzniklé v membránách se zvýšeným množstvím sfingomyelinu (ve srovnání s a)), jejichž velikost se nemění během titrace dodatečným CTxB a k nimž se CTxB váže méně pevně.

Hesla

Elektronický přenos/migrace energie, FRET, FCS, Monte Carlo simulace, relaxace rozpouštědla, lipidová dvojvrstva, rafty, micely, BODIPY, fázový diagram.

Jazyk: Angličtina

ISBN: 978-91-7459-390-7

Počet stránek: 46 + 7 publikací

This thesis has been elaborated within the framework of the Agreement on Joint Supervision (co-tutelle) of an International Doctoral Degree Programme between Charles University in Prague, Czech Republic and the Department of Chemistry at Umeå University, Sweden.

I declare that I have elaborated the thesis on my own. Other already published results used in this thesis are included in the list of references. The thesis or a substantial part of it has not been used elsewhere for receiving the same or a different academic title.

In Prague, 2011-11-11

Radek Šachl

CONTENTS

ABBREVIATIONS.....	vii
LIST OF PAPERS.....	viii
1. INTRODUCTION.....	1
2. THEORETICAL BACKGROUND.....	3
2.1 Fluorescence.....	3
2.2 Fluorescence anisotropy.....	3
2.3 Measurement of steady-state & time-resolved fluorescence.....	5
2.4 Electronic energy transfer/migration within a pair.....	6
2.5 FRET/DDEM within an ensemble of fluorescent molecules.....	8
2.6 FRET/DDEM in a lipid bilayer.....	9
2.7 Measurements of donor-donor energy migration.....	10
2.8 Monte Carlo simulations of FRET in lipid systems.....	11
2.9 Fluorescence Solvent Relaxation (SR).....	12
2.10 Fluorescence correlation spectroscopy (FCS).....	14
2.11 Suitable fluorescence probes for FRET/DDEM/SR experiments.....	15
3. RESULTS AND DISCUSSION.....	17
3.1 The localisation of fluorescent probes.....	17
3.1.1 Do methylated-BODIPY groups when attached at the end of long acyl chains loop back to the lipid-water interface (paper III)?.....	17
3.1.2 Do the conical like BODIPY probes preferentially locate in bilayers with high curvature (paper V)?.....	21
3.1.3 Solvation dynamics of fluorescent probes PRODAN and LAURDAN in PCL-PEO vesicles (paper I).....	24
3.1.4 Localisation of 2-pyridones in G _{M1} micelles (paper IV).....	27
3.2 Lipid nanodomain size estimation.....	29
3.2.1 What are the limitations of FRET in lipid nanodomain size estimation (paper VI)?.....	30
3.2.2 Is nanodomain formation preceding microscopic phase separation (paper VII)?.....	32
3.2.3 Self-assembly of G _{M1} ganglioside molecules water (paper II).....	36
4. CONCLUSIONS.....	39
5. ACKNOWLEDGEMENTS.....	42
6. REFERENCES.....	43

ABBREVIATIONS

2-AS = 2-(9-anthroyloxy)-stearic acid

A = acceptor

B-F = Baumann-Fayer

BnPC = *sn*-2-acyl labelled phosphatidylcholine with *n* carbons in the *sn*-2 chain bearing Me⁴-BODIPY group

C₂ = reduced surface concentration

CTxB = cholera toxin

D = donor

DDEM = donor-donor energy migration

DOPC = 1,2-dioleoyl-*sn*-glycero-3-phosphocholine

DOPG = 1,2-dioleoyl-*sn*-glycero-3-phospho-(1'-*rac*-glycerol) (sodium salt)

DPPC = 1,2-dipalmitoyl-*sn*-glycero-3-phosphocholine

DSPE-PEG2000 = 1,2-distearoyl-*sn*-glycero-3-phosphoethanolamine-N-[methoxy (polyethylene glycol)-2000] (ammonium salt)

dPE = 1,2-dipalmitoyl-*sn*-glycero-3-phosphoethanolamine

F(*t*) = time-resolved fluorescence intensity

FCS = fluorescence correlation spectroscopy

FL-BODIPY = 4,4-difluoro-4-bora-3a,4a-diaza-5,7-dimethyl-*s*-indacenyl

564/570-BODIPY = 4,4-difluoro-4-bora-3a,4a-diaza-5-styryl-dimethyl-*s*-indacenyl

FRET = Förster resonance energy transfer

G(*t*) = probability that the previously excited donor is still in the excited state

g^{FCS}(*t*) = autocorrelation function obtained by FCS

K_i = distribution constant given by the concentration of the probe in the domains/curved regions and in the remaining/planar part of the bilayer

Me⁴-BODIPY = 4,4-difluoro-1-3-5-7-tetra-methyl-4-bora-3a,4a-diaza-*s*-indacene-8-yl

MC = Monte Carlo

mPE = 1-palmitoyl-2-hydroxy-*sn*-glycero-3-phosphoethanolamine

PCL-PEO = poly(ϵ -caprolacton)-*block*-poly(ethylene oxide)

r(*t*) = time-resolved anisotropy

R₀ = Förster radius

Sph = Sphingomyelin

SR = solvent relaxation

LIST OF PAPERS

The thesis is based on the following papers:

- I. Šachl, R., Štěpánek, M., Procházka, K., Humpolíčková, J., Hof, M.; Fluorescence Study of the Solvation of Fluorescent Probes Prodan and Laurdan in Poly(ε -caprolactone)-*block*-poly(ethylene oxide) Vesicles in Aqueous Solutions with Tetrahydrofuran *Langmuir* **2008**, 24, 288-295.
- II. Šachl, R., Mikhalyov, I., Hof, M., Johansson, L.B.-Å.; A comparative study on ganglioside micelles using electronic energy transfer, fluorescence correlation spectroscopy and light scattering techniques *PCCP* **2009**, 11(21), 4335.
- III. Šachl, R., Boldyrev, I., Johansson, L.B.-Å.; Localisation of BODIPY labelled phosphatidylcholines in lipid bilayers, *PCCP* **2010**, 12(23), 6027.
- IV. Šachl, R., Rosenbaum, E., Sellstedt, M., Almquist, F., Johansson, L.B.-Å.; Locations and Reorientations of Multi-ring-fused 2-Pyridones in Ganglioside G_{M1} micelles, *Langmuir* **2011**, 27, 1662.
- V. Šachl, R., Mikhalyov, I., Gretskaya, N., Olzynska, A., Hof, M., Johansson, L.B.-Å.; Distribution of BODIPY-labelled phosphatidylethanolamines in lipid bilayers exhibiting different curvatures, *PCCP* **2011**, 13, 11694.
- VI. Šachl, R., Humpolíčková, J., Štefl, M., Johansson, L.B.-Å., Hof, M.; Limitations of Electronic Energy Transfer in Lipid Nanodomain Size Estimation, *Biophys. J.* **2011**, 101, L60-L62.
- VII. Štefl, M., Šachl, R., Humpolíčková, J., Cebecauer, M., Macháň, R., Johansson, L.B.-Å., Hof, M.; Dynamics and Size of Crosslinking-Induced Lipid Nanodomains in Model Membranes, submitted to *Biophys. J.* **2012**.

Other papers which are not included in the thesis:

- Šachl, R., Uchman M., Matějíček, P., Procházka, K., Štěpánek, M.; Preparation and Characterization of Self-assembled Nanoparticles Formed by Poly(ethylene oxide)-*block*-poly(ε -caprolactone) Copolymers with Long Poly(ε -caprolactone) Blocks in Aqueous Solutions *Langmuir* **2007**, 23, 3395.

- Mikaelsson, T., Šachl, R., Johansson, L.B.-Å.; Electronic Energy Transport and Fluorescence Spectroscopy for Structural Insight into Proteins, Regular Protein Aggregates and Lipid Systems *Reviews in Fluorescence 2007* **2009**, 4, 53.
- Procházka, K., Matějíček, P., Štěpánek, M., Limpouchová, Z., Hof, M., Humpolíčková, J., Šachl, R., Schroeder, J.; Solvent relaxation studies applied to stimuli-responsive core-shell nanoparticles, *Proceedings of SPIE* **2010**, 7571.
- Procházka, K., Limpouchová, Z., Uhlík, F., Košovan, P., Matějíček, P., Štěpánek, M., Uchman, M., Kuldová, J., Šachl, R., Humpolíčková, J., Hof, M.; Fluorescence Spectroscopy as a Tool for Investigating the Self-Organized Polyelectrolyte Systems, *Adv Pol Sci* **2011**, 241/2011, 187-249.

1.INTRODUCTION

A cell membrane is a very complex system, which is build up by various kinds of lipids and proteins. In order to understand the complicated membrane biophysics it is convenient to focus on model systems primarily, which still resemble the object of interest but do not contain so many interacting compounds. Commonly used model systems are i) large/giant unilamellar lipid vesicles, ii) supported phospholipid bilayers¹ and recently iii) bicelles^{2,3}, whose shape resembles a disc with highly curved rims. The biophysics of such simple systems is complicated and not fully understood yet. For instance, bilayers composed of only three lipids, DOPC, sphingomyelin and cholesterol,⁴ can be found in several physical states depending on the ratio between the three lipids: these are liquid-disordered, liquid ordered or gel phases, as well as two or more phases coexisting with each other. Recently, such a coexisting region has been studied⁵⁻⁸ and it is mostly connected with the formation of microscopic (and possibly also nanoscopic) liquid ordered domains (\approx rafts, *cf.* section 3.2).

Even when the bilayer forms a homogenous phase it exhibits a steep gradient in physical properties perpendicular to the interface. The bilayer is more polar and less viscous close to the interface while its interior is hydrophobic.⁹ This phenomenon leads to a preferential localisation of hydrophobic compounds in the interior¹⁰ whereas more polar compounds accumulate close to the lipid-water interface (*cf.* paper III). The localisation of fluorescent probes represents no exception to this. Since fluorescent probes solely report on properties of their immediate vicinity knowledge about the probe location is substantial. As will be shown in the thesis, the localisation of probes within the bilayer may also very strongly influence the resolution when measuring the sizes of lipid nanodomains (paper VI).

The thesis is divided into two major parts. The first part concerns the localisation of probes in lipid/polymeric bilayers and in G_{M1} micelles. Paper III introduces a method based on electronic energy transfer/migration which can efficiently determine the transversal position of fluorescence molecules in bilayers. Utilization of this technique is demonstrated by positioning newly synthesized BODIPY probes in the DOPC bilayer. In paper V we continued the previous study and showed that a combination of Förster resonance energy transfer (FRET) with Monte Carlo simulations enables the localisation of probes in bicelles and in bilayers containing pores, *i.e.* in lipid systems with variable curvature. This approach has been used to test whether conical-like fluorescence probes have increased affinity to highly curved regions, which would enable preferential labelling of membrane pores.

In the second part we characterized the dynamics and the size of lipid subdiffraction-sized domains in model membranes, containing a variable amount of cholera toxin and sphingomyelin. More specifically, in paper VII we show limitations of FRET in the determination of lipid nanodomain sizes. Interestingly, these limitations originate from

the lack of probes with high affinity to the liquid-ordered domain phase. In paper VI we provide a detailed dynamic and structural study of a crosslinker-triggered formation of nanodomains. By using FRET and z-scan fluorescence correlation spectroscopy, we revealed two types of nanodomains and hypothesize that the lack of sphingomyelin in the bilayer with the particular composition can be compensated by increasing the levels of the crosslinker CTxB.

The submitted thesis is a result of a successful collaboration between the group of Martin Hof in Prague and the group of Lennart B.-Å. Johansson in Umeå. The former group has developed state of the art fluorescence techniques and mainly applies these to various biological questions. One of the frequently applied techniques is the solvent relaxation technique, which is capable of detecting physiologically relevant changes in phospholipid bilayers. The group has also contributed considerably to the application and development of fluorescence correlation spectroscopy. The latter group has established the donor-donor energy migration as a new technique in biomembrane and protein research. The achievements have been based on the development of theory, as well as the synthesis and/or modification of fluorescent lipids or proteins. This thesis aims at combining the expertise and ideas of both teams and focuses on solving biophysical questions by using a broad spectrum of modern fluorescence techniques.

2. THEORETICAL BACKGROUND

2.1 Fluorescence^{11, 12}

A relatively rigid molecule has a tendency to return to its electronic ground state (S_0) by the emission of a photon. For excitation transitions occurring within the Franck-Condon approximation the absorption is fast (10^{-15} s) whereby the nuclei do not move during the absorption process. Typically, the excited molecule relaxes within 10^{-12} - 10^{-10} s to the first electronic excited state S_1 . The lifetime corresponding to radiative relaxation ranges from 10^{-10} to 10^{-7} s. After that the molecule returns to one of the vibrational levels of electronic ground state S_0 by emitting a photon. Fluorescence is a spin-allowed transition as opposed to phosphorescence, which is spin-forbidden, and thus occurs much slower.

When a large ensemble of molecules is considered, the decay rate of the excited molecules can be expressed as in chemical kinetics by the following differential equation¹²

$$-\frac{dN(t)}{dt} = (k_r + k_{nr})N(t)^*, \quad (2.1.1)$$

where $N(t)^*$ is the number of molecules in the excited state S_1 and k_r or k_{nr} are the rate constants for radiative or nonradiative deactivation, respectively. Since the fluorescence intensity $F(t)$ is proportional to the number of excited molecules, one obtains that

$$F(t) = k_r N(t)^* = k_r N_0^* \exp(-t/\tau), \quad (2.1.2)$$

where N_0^* is the number of excited molecules at time 0 and $\tau (= \frac{1}{k_r + k_{nr}})$ the lifetime of the S_1 state. Unfortunately, the fluorophores may not exhibit single-exponential decays and the decay curves need to be described according to

$$F(t) = \sum_i \alpha_i \exp(-t/\tau_i). \quad (2.1.3)$$

Here α_i & τ_i denote amplitudes & lifetimes of the S_1 state, respectively. Deviations from Eq. 2.1.2 are often due to different environments of the fluorophores, by excited state reactions or by relaxation of the surrounding of the excited probe.¹²

2.2 Fluorescence anisotropy

The probability (P) that molecules with the absorption transition moment $\vec{\mu}_A$ will be excited by the electric field vector \vec{E} of the incident light depends on the angle θ_A between these vectors, *i.e.* $P \approx \cos^2 \theta_A$. Thus, the excitation of isotropically oriented

molecules by polarised light leads to a preferential excitation of molecules whose absorption transition dipole moments are oriented parallel to \vec{E} . This phenomenon is called photoselection¹² and provides an anisotropic emission of fluorophores. Since the excited molecules usually reorient prior to the emission of any photon the anisotropic distribution of the excited molecules decreases in time. As will be shown here, other processes may also contribute to the depolarisation.

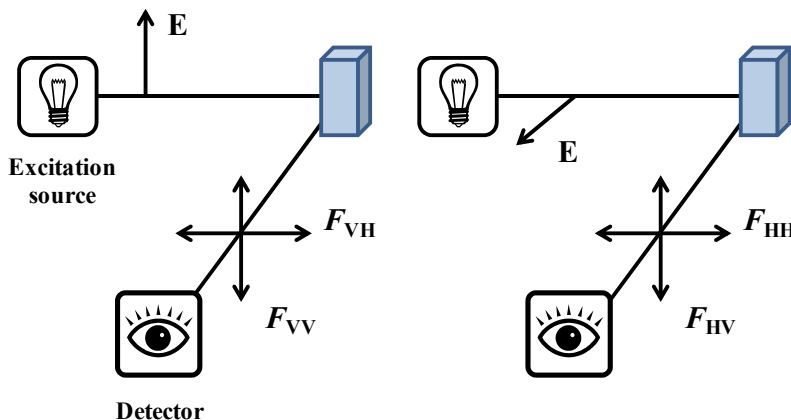
A characterization of the polarisation of fluorescence is called the anisotropy and is defined by measured intensities F_{VV} and F_{VH} as

$$r(t) = \frac{F_{VV}(t) - gF_{VH}(t)}{F_{VV}(t) + 2gF_{VH}(t)}. \quad (2.2.1)$$

The indices VV and VH refer to excitation by vertically polarised light and detection of the emission under vertical or horizontal alignments of the emission polariser, respectively (*cf.* Picture 2.1.1). The intensity $F_{VV}(t) + 2gF_{VH}(t)$ is directly proportional to the total fluorescence emission. The correcting factor g accounts for the non-ideality of the optical instrumentation, which mostly originates from the fact that the vertical and horizontal light components are transmitted through the fluorescence spectrometer with different efficiency. It can be shown that $r(t)$ is related to the reorienting motions of the emission transition dipole moments of the probes $\vec{\mu}$ via¹²

$$r(t) = r_0 \langle P_2[\vec{\mu}(0) \cdot \vec{\mu}(t)] \rangle. \quad (2.2.2)$$

Here P_2 stands for the second rank Legendre polynomial $(3x^2-1)/2$ and r_0 is the fundamental anisotropy,¹¹ *i.e.* the anisotropy in the absence of any reorienting motions. The brackets $\langle \dots \rangle$ indicate an ensemble average over all excited molecules.



Picture 2.1.1: Excitation of the sample by either vertically (left) or horizontally (right) polarized light. Emission is observed by using a vertically or horizontally aligned polarizer.

In the case of a freely reorienting molecule, which is approximated by a spherical particle with a rotational diffusion coefficient D_{rot} the anisotropy r decays monoexponentially^{11, 12}

$$r(t) = r_0 \exp(-6D_{rot}t). \quad (2.2.3)$$

The anisotropy decay of non-spherical fluorophores dissolved in the bulk can be described by the sum of five exponentials.¹¹ When the fluorophore is attached to a larger molecule and/or the molecule rotates in an anisotropic medium the reorientation may be sterically hindered, *i.e.* the transition dipole moments do not become isotropically oriented ($\lim_{t \rightarrow \infty} r(t) \neq 0$).¹¹ Then the anisotropy decay can be expressed as

$$r(t) = \sum_j A_j \exp(-\theta_j t) + r_\infty; \quad \sum_j A_j = r_0 - r_\infty, \quad (2.2.4)$$

where A_j are preexponential factors, θ_j rotational correlation times and r_∞ the limiting anisotropy.

2.3 Measurement of the steady-state & time-resolved fluorescence

Steady-state measurements The fluorescence or emission spectrum, $S(\lambda_F)$ reflects the probability distribution of different transitions from the lowest vibrational level of the S_1 state to the various vibrational levels of the S_0 state. In practice, one measures the fluorescence intensity, $F(\lambda_E, \lambda_F)$, at a fixed excitation wavelength (λ_E) as a function of the emission wavelength (λ_F),

$$F(\lambda_E, \lambda_F) = k I_A(\lambda_E) S(\lambda_F), \quad (2.3.1)$$

where I_A is the intensity of absorbed light, and the proportionality factor k depends on the optical configuration of the fluorometer and bandwidths of the monochromator. In order to monitor the intensity, which is proportional to the total intensity $I_{VV} + 2I_{VH}$ (and thus is independent of molecular reorientations), a vertically aligned polariser is placed into the excitation light path whereas a polariser oriented at the magic angle 54.7° relative to the former is inserted into the emission path.

The steady-state anisotropy r_s , which is related to $r(t)$ by

$$r_s = \frac{\int_0^\infty F(t)r(t)dt}{\int_0^\infty F(t)dt} = \frac{F_{VV}-gF_{VH}}{F_{VV}+2gF_{VH}}. \quad (2.3.2)$$

is one of the results in steady-state measurements. In order to calculate r_s the continuous (*i.e.* time-independent) fluorescence intensities F_{VH} , F_{VV} , F_{HH} and F_{HV} must be recorded. The two latter intensities are used to calculate the g -factor, *i.e.* $g = F_{HH}/F_{HV}$ (*cf.* Picture 2.1.1). When exciting the sample with horizontally polarised light the only difference between F_{HH} and F_{HV} , *i.e.* between intensities observed for horizontal and vertical alignment of the emission polariser, originates from the non-ideality of the optical transmission (see above).

Time-resolved measurements were based on the *time-correlated single photon counting* (TCSPC) method,^{11, 12} which relies on the repeated detection of the first emitted photon at time t after an excitation pulse. A sensitive photomultiplier detects the first arriving photon after the excitation pulse. After the photon is registered, the content of a memory channel corresponding to the time between the excitation pulse and the registration of the photon is increased by one. The detection of a sufficient amount of photons (around 25.000 at the maximum) is required in order to obtain representative decay curves.

Because the pulse profile of a flash lamp or laser is not infinitively short as compared to the fluorescence decay $F(t)$ is a result of a convolution between the fluorescence decay $f(t)$ and the excitation profile $L(t)$

$$F(t) = \int_0^t L(t')f(t - t')dt. \quad (2.3.3)$$

For estimating the $f(t)$, a deconvolution procedure needs to be carried out. This involves a numerical minimization of the expression

$$\chi^2 = \frac{1}{v} \sum_{i=1}^N \left(\frac{R(t_i) - R_c(t_i)}{\sigma_i} \right)^2. \quad (2.3.4)$$

In Eq. 2.3.4 v is the number of degrees of freedom, $R_c(t_i)$ is the fit of the function $R(t_i)$ obtained after convolution of $f(t)$ with $L(t)$ and σ_i is the standard deviation.

2.4 Electronic energy transfer/migration within a pair

Förster resonance energy transfer (FRET) is a nonradiative transfer of the excitation energy from a donor to an acceptor molecule, and it is the result of a long-range dipole–dipole interaction within the donor-acceptor pair. The quantum-mechanical description of the phenomenon was firstly derived by Theodor Förster, who showed that the rate ω depends on the separation distance R between the donor and acceptor,¹³ respectively.

$$\omega = \frac{3\langle\kappa^2\rangle}{2\tau_D} \left(\frac{R_0}{R} \right)^6. \quad (2.4.1)$$

Here $\langle\kappa^2\rangle$, τ_D and R_0 denote the mean square average of the angular part of the dipole-dipole interaction, the donor lifetime in the absence of an acceptor and the Förster radius,¹¹ respectively

$$R_0^6 = \frac{9000 \ln(10)(2/3)Q_D}{128\pi^5 n^4 N_A} \int_0^\infty F_D(\lambda) \epsilon_A(\lambda) \lambda^4 d\lambda. \quad (2.4.2)$$

As follows from this equation, the FRET rate is also influenced by the quantum yield of the donor Q_D , the refractive index of the medium n and the overlap integral $J = \int_0^\infty F_D(\lambda) \varepsilon_A(\lambda) \lambda^4 d\lambda$. The latter refers to the extent of overlap between the donor fluorescence spectrum $F_D(\lambda)$ and the acceptor absorption spectrum $\varepsilon_A(\lambda)$. The symbols N_A and λ refer to the Avogadro constant and the wavelength of light, respectively.

It is convenient to introduce a unit which reports on the efficiency of FRET. The efficiency (E) is defined by the rate constant for FRET (k_T) and the radiative deexcitation ($k_r = 1/\tau_D$) according to

$$E = \frac{k_T}{k_T + k_r} = \frac{R_0^6}{R_0^6 + R^6}. \quad (2.4.3)$$

Due to the sixth power dependence of E on R the FRET efficiency is the most sensitive to R when $R \approx R_0$. For values of $R < R_0/2$, E approaches unity whereas for $R > 2R_0$, E reaches zero with increasing R . Thus, the highest sensitivity of FRET in the distance estimation depends on typical values of R_0 (20-100 Å). Fortunately, these distances correspond to typical dimensions of various biological self-assemblies, or to *intra-* and *inter*-protein distances.

For donors being excited in the presence of an acceptor there are two possible relaxation pathways of the excitation energy. The donor could emit a photon – as would be the case in the absence of an acceptor, or radiation-less transfer of the excitation energy to the acceptor. Consequently, the fluorescence decay of the donor in the presence of an acceptor becomes faster. It can be shown that the fluorescence intensity decays according to¹²

$$F(t) = F_D(t) \exp(-\omega t), \quad (2.4.4)$$

where $F_D(t)$ represents the decay in the absence of FRET.

The presented equations have so far neglected the influence of reorienting motions on energy transfer. This is valid when the probes reorient much faster as compared to the time scale of energy transfer. Then, the κ^2 factor is averaged prior to energy transfer and equals 2/3. The reorienting motions enter the equation by means of the reorienting factor κ^2

$$\kappa^2 = [\vec{\mu}_1 \cdot \vec{\mu}_2 - 3(\vec{\mu}_1 \cdot \vec{R})(\vec{\mu}_2 \cdot \vec{R})]^2. \quad (2.4.5)$$

In this equation $\vec{\mu}_i$ and \vec{R} denote unit vectors of the transition dipole moment of the donor/ acceptor and the vector connecting the interacting molecules, respectively. If the motions occur on a similar time-scale as FRET, the energy transfer rate becomes time-dependent due to reorienting motions. However, an extended Förster theory accounts for this complication and provides the following relation¹⁴

$$F^{\text{EFT}}(t) = F_D(t) \langle \exp\left(-\int_0^t \omega(t') dt'\right) \rangle. \quad (2.4.6)$$

The expression within the brackets denotes a stochastic average over the rates of electronic energy transfer between a donor and an acceptor forming a DA pair. It can be shown that Eq. 2.4.6 is transferred into 2.4.4 in the limit of short times ($\lim_{t \rightarrow 0} F^{\text{EFT}}(t) = F_D(t) \exp(-\langle \omega \rangle t)$).¹⁴

2.5 FRET/DDEM within an ensemble of fluorescent molecules

According to the Bauman and Fayer model, the energy transfer/migration within an ensemble of fluorescent molecules can be described within the two particle approximation.¹⁵ In the case of DDEM the energy is allowed to jump from the excited donor to an unexcited one and then back. However, the energy cannot be transferred via the previously unexcited molecule further to another unexcited donor.

FRET. For describing FRET in a system where the excited energy can be transferred to more than one acceptor, it is convenient to introduce the probability $G(t)$, which provides the probability that the initially excited donor is still in the excited state after a time t . Then the decay $F(t)$ of a donor surrounded by acceptors is given by

$$F(t) = G_{\text{DA}}(t) \sum_i \alpha_i \exp(-t/\tau_i), \quad (2.5.1)$$

where $\sum_i \alpha_i \exp(-t/\tau_i)$ represents the decay of a donor in the absence of FRET. Now consider a lattice where the probability of occupancy of each site is p , and that all pairwise interactions between the excited donor and any acceptor are independent. Then each site surrounding the donor is empty with the probability of $1-p$. Such a vacant site contributes to the $G(t)$ function by $1-p$. On the other hand, an occupied site contributes to $G(t)$ by $pe^{-\omega_i(r_i)t}$, where $\omega_i(r_i)$ is the energy transfer rate for the i^{th} acceptor. Taken together $G(t)$ can be expressed as

$$G_{\text{DA}}(t) = \prod_{i=1}^N [(1-p) + pe^{-\omega_i(r_i)t}]. \quad (2.5.2)$$

Expanding the logarithm of Eq. 2.5.2 in powers of p yields

$$\ln G_{\text{DA}}(t) = - \sum_{k=1}^{\infty} \frac{p^k}{k} \sum_{i=1}^N [1 - e^{-\omega_i(r_i)t}]^k. \quad (2.5.3)$$

Because p is usually very low one can keep only the first term in the expansion with $k = 1$. Furthermore, the summation is replaced by integration over space, *i.e.* a homogenous spatial distribution of acceptors $u(r)$ is assumed, where p turns into a number density ρ . Eq. 2.5.3 can be written as

$$\ln G_{\text{DA}}(t) = -\rho \int_0^\infty (1 - e^{-\omega(r)t}) u(r) dr. \quad (2.5.4)$$

In the dynamic limit, in which the molecules reorient much faster as compared to an energy transfer event, ω can be averaged before any transfer occurs, and therefore becomes time-independent. However, this needs not be true, since reorienting motions may occur on the same time scale as FRET, or even slower. Nevertheless, the dynamic limit approximation is reasonable approximation for an ensemble of acceptors surrounding a donor, where the excited donor senses an average electrostatic field of acceptors, taking up all possible orientations at the instant of the energy transfer event.

DDEM. Here one can proceed similarly as for DAET, which leads to

$$\ln G_{\text{DD}}(t) = -\frac{\rho}{2} \int_0^\infty (1 - e^{-2\omega(r)t}) u(r) dr. \quad (2.5.5)$$

Eqs. 2.5.4 and 2.5.5 are similar and can thus be combined into one equation by introducing a factor λ , which is equal 1 for FRET and 2 for DDEM

$$\ln G(t) = -\frac{\rho}{\lambda} \int_0^\infty \left(1 - e^{-\frac{3}{2}\lambda \left(\frac{R_0}{R}\right)^6 \langle \kappa^2 \rangle \frac{t}{\tau}} \right) u(r) dr. \quad (2.5.6)$$

2.6 FRET/DDEM in a lipid bilayer

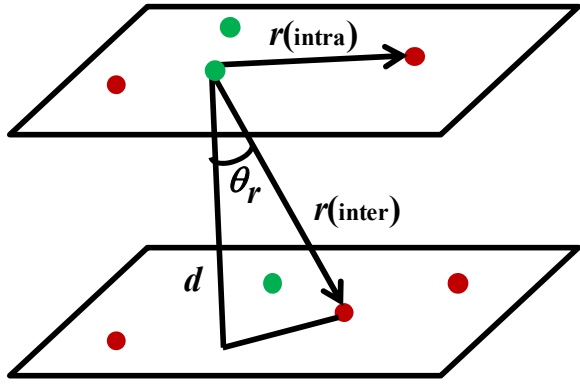
In a lipid bilayer the excitation energy can be transferred either to a molecule localised in the same leaflet, or to one in the opposite leaflet. In the former process, $G_{\text{intra}}(t)$ is referred to as *intra*-FRET while the latter one $G_{\text{inter}}(t)$ is called *inter*-FRET. The total survival probability $G_{\text{tot}}(t)$ is given by the joint probability according to

$$G_{\text{tot}}(t) = \prod_j G_{j,\text{inter/intra}}(t). \quad (2.6.1)$$

FRET/DDEM within a plane. In this case the spatial distribution function is given by $u(r) = 2\pi r$. By introducing the substitutions $\mu = \lambda \frac{3}{2} R_0^6 \langle \kappa^2 \rangle \frac{t}{\tau}$, $y = \frac{\mu}{r^6}$ and $C_2 = \pi R_0^2 \rho$ Eq. 2.5.4 transforms into the final form¹⁵

$$\begin{aligned} \ln G_{\text{intra}}(t) &= -\frac{\pi}{3\lambda} \rho \mu^{\frac{1}{3}} \int_0^\infty (1 - e^{-y}) y^{-\frac{4}{3}} dy = \\ &= -C_2 \lambda^{-2/3} \Gamma\left(\frac{2}{3}\right) \left(\frac{t}{\tau}\right)^{1/3}. \end{aligned} \quad (2.6.2)$$

C_2 is a so-called reduced surface concentration and equals the number of acceptor molecules found in the area of a circle with the radius R_0 surrounding a donor. The integral in Eq. 2.6.2 is tabulated and equals $\Gamma(2/3)$.



Picture 2.6.1: Intra- and inter-energy transfer from donors (green spheres) to acceptors (red spheres) in a lipid bilayer. R denotes the distance between D/A, d the bilayer thickness and θ_r the angle between the bilayer normal and the vector connecting D/A.

FRET/DDEM between two parallel planes. The planes are separated by the distance d . In this case it is convenient to perform the integration over θ_r , the angle between the bilayer normal and the vector connecting the donor and the acceptor. By using the spatial distribution $u(r) = 2\pi d^2 \frac{\sin \theta_r}{\cos^3 \theta_r}$ Eq. 2.5.6 is given as¹⁵

$$\ln G_{\text{inter}}(t) = -\frac{2\pi d^2}{\lambda} \rho \int_0^{\pi/2} \left\{ 1 - \exp \left[-\frac{3}{2} \lambda \left(\frac{R_0}{d} \right)^6 \cos^6 \theta_r \langle \kappa^2 \rangle \frac{t}{\tau} \right] \right\} \frac{\sin \theta_r}{\cos^3 \theta_r} d\theta_r. \quad (2.6.3)$$

By inserting $s = \frac{3}{2} \lambda \left(\frac{R_0}{d} \right)^6 \cos^6 \theta_r \langle \kappa^2 \rangle \frac{t}{\tau} = \nu \langle \kappa^2 \rangle \cos^6 \theta_r$ one finally obtains¹⁵

$$\ln G_{\text{inter}}(t) = -\frac{c_2}{3} \left(\frac{d}{R_0} \right)^2 \left(\frac{2\nu}{3} \right)^{1/3} \int_0^{\langle \kappa^2 \rangle \nu} (1 - e^{-s}) s^{-4/3} ds. \quad (2.6.4)$$

Due to the singularity at $s = 0$, the integral was numerically evaluated by increasing the negative $s^{-4/3}$ power to a positive value by using a two step partial integration

$$\ln G_{\text{inter}} = \frac{c_2}{\lambda} \left(\frac{d}{R_0} \right)^2 \left[1 - e^{-2/3\nu} (1 + \nu) - \frac{3}{2} \left(\frac{2}{3} \nu \right)^{1/3} \int_0^{\langle \kappa^2 \rangle \nu} e^{-s} s^{2/3} ds \right]. \quad (2.6.5)$$

In order to fasten the numerical evaluation, several asymptotic relations are relevant for limiting values of ν , *i.e.* either for short or long times as compared to τ .¹⁵

2.7 Measurements of donor-donor energy migration

Since the measurement of the photophysics of the donor is not influenced by DDEM (in contrast to FRET, *cf.* Eq. 2.5.1) the process of energy migration cannot be detected by simple measurements of the donor fluorescence decay. Instead, one has to carry out more time-consuming depolarisation experiments, which are based on the fact that

energy migration among donors leads to a loss in polarisation.^{11, 12} However, there exists no analytical equation which precisely accounts for DDEM within an ensemble of donors. In order to analyze the DDEM in a lipid bilayer we used the following phenomenological equation

$$r(t) = G_{\text{tot}}(t)[r_{\text{rot}}(t) - r_{\infty}] + r_{\infty}, \quad (2.7.1)$$

where $r_{\text{rot}}(t)$ denotes the rotational and r_{∞} the limiting anisotropy. According to¹⁶ this equation provides a reasonable agreement with Monte Carlo simulations. The equation involves a few limitations: 1. Energy migration and reorienting motions must occur on a different time-scale (see also above); 2. light emitted by another than the previously excited molecule is completely depolarized and 3. the limitations following from the two-particle approximation (see above).

2.8 Monte Carlo simulations of FRET in lipid systems

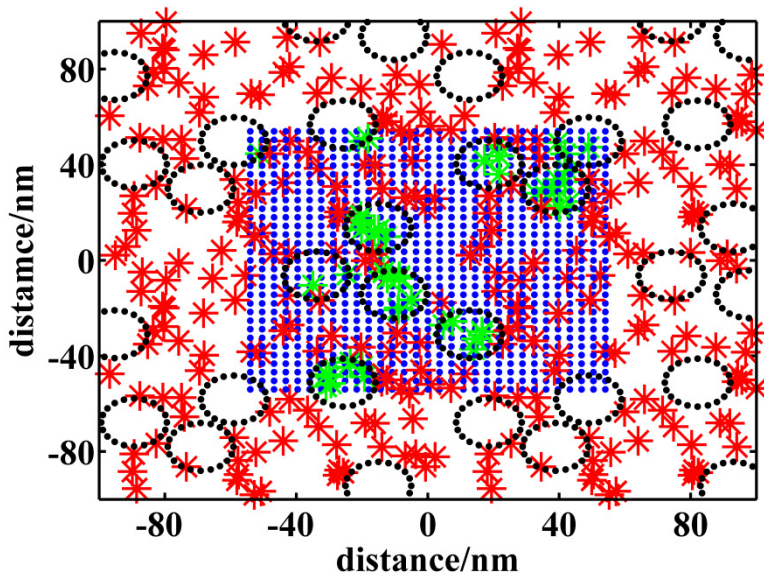
Analytical equations describing FRET/DDEM are complex and exist only for a limited number of basic geometries. To circumvent this it is convenient to instead apply Monte Carlo simulations,¹⁶⁻¹⁸ which can successively mimic various random processes. We have used this approach to describe FRET in lipid bilayers containing circular nanodomains (*cf.* papers VI, VII), toroidal pores (*cf.* paper V), as well as in lipid bicelles (*cf.* paper V). The following steps have been carried out: (i) For pore/nanodomain containing membranes, a certain number of pores/domains were generated (*cf.* Picture 2.8.1), which corresponded to a pre-defined peptide to lipid ratio in the case of pores, and to the area fraction of the domains occupied in the bilayer in the case of domains. (ii) The donors and acceptors were generated to exhibit a certain probability of localisation within and outside the pores, domains and bicellar rims. The distribution was described by an equilibrium constant K_d (= [probes within]/[probes outside]). (iii) A donor was randomly excited and assumed to transfer its excitation energy to an acceptor. The time for this event to occur depends on the overall energy transfer rate Ω_i according to¹⁶

$$\Delta t_i = -\ln \alpha / \Omega_i, \quad (2.8.1)$$

where α denotes a random number between 0-1. The total energy transfer rate is calculated as a sum of energy transfer rates from the excited donor i to all acceptors. Acceptors that are beyond the cut-off distance $10R_0$ are included via the continuum approach¹⁶

$$\Omega_i = \sum_j \frac{3}{2} \kappa_{ij}^2 \left(\frac{R_0}{R_{ij}} \right)^6 \tau_D^{-1} + C_2 \left(\frac{R_0}{R_c} \right)^4 \tau_D^{-1}. \quad (2.8.2)$$

Here j ($1 \leq j \leq N$) refers to the number of acceptors (N) found within a cut-off distance R_c . R_{ij} is the distance between the i -th donor and j -th acceptor. The second term in Eq. 2.8.2 accounts for rates between the excited donor and the continuum of acceptors for two parallel planes (*i.e.* for a model lipid bilayer). The simulations correspond to energy transfer taking place under the dynamic limit condition and among isotropically oriented donors and acceptors. Therefore, kappa factor $\langle \kappa_{ij}^2 \rangle = 2/3$. New configurations were generated approximately 3000 times, whereas each generated configuration set was used 100 times in the calculation step. Periodic boundary conditions were used in order to imitate the infinitely large membrane containing pores/domains. The dimensions of the replicated box were $20R_0 \times 20R_0$. The outcome of the simulation is the $G(t)$ function, which is related to the fluorescence decay *via* Eq. 2.5.1. Since FRET occurs within a few nanoseconds it was not necessary to involve diffusion of probes across the bilayer within the simulation time. The reorientation dynamics of the fluorescent probes was not assumed to exist because of the above mentioned reasons.



Picture 2.8.1: The distribution of donors (green stars) with $K_D = 1000$ and acceptors with $K_A = 0.001$ (red stars) on a bilayer containing circular nanodomains (black dots). The replicated part of the bilayer is showed by the blue dots.

2.9 Fluorescence solvent relaxation (SR)^{9, 19, 20}

The absorption of a photon by a molecule occurs almost instantaneously as compared to the rate of molecular motions and within a time period of ca. 10^{-15} s results in an immediate change in the molecular dipole moment. The surrounding polar solvent molecules respond to this change by reorientation, leading to a minimization of the excited state energy. Consequently, molecules which reorient slowly - as is the case for molecules dissolved in a viscous medium – will emit from a non-relaxed excited state with higher energy, whereas molecules which reorient faster in a less viscous medium mostly emit from a relaxed equilibrated state. Depending on the

microviscosity of the environment the steady-state fluorescence spectra are red or blue shifted. Since the Stokes frequency shift is related to the energy decrease of the excited fluorophore this shift in spectra also monitors the micropolarity of the environment.

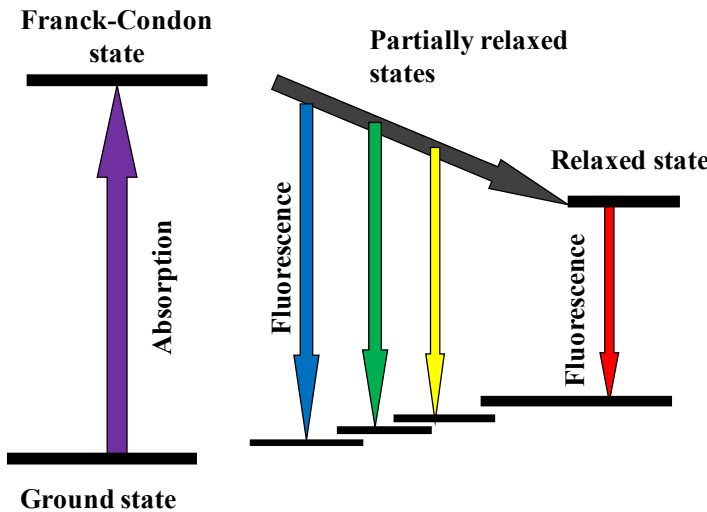
By monitoring fluorescence decays $D(\lambda, t)$ as a function of the emission wavelength together with the corresponding steady-state spectrum $S(\lambda)$ it is possible to construct time-resolved fluorescence spectra, *i.e.* emission spectra at an arbitrary time after excitation

$$F(\lambda, t) = \frac{D(\lambda, t)S(\lambda)}{\int_0^\infty D(\lambda, t)dt}. \quad (2.9.1)$$

The time-evolution of the peak maximum of the determined frequency time-resolved emission spectra ν_{\max} reflects the mobility of the solvent molecules surrounding the excited fluorophore (*i.e.* viscosity of the microenvironment). The solvation dynamics is effectively characterized by a correlation function $C(t)$

$$C(t) = \frac{\nu_{\max}(t) - \nu_{\max}(\infty)}{\nu_{\max}(0) - \nu_{\max}(\infty)}. \quad (2.9.2)$$

The position of the frequency maximum ($\nu_{\max}(0)$) at the time of excitation $t = 0$ is not directly measurable, but can be estimated.⁹ Evaluation of $\nu_{\max}(0)$ reveals the part of the relaxation process which is beyond the resolution of the equipment.



Picture 2.9.1: The principle of the solvent relaxation technique, which is based on the minimization of the excited state energy, mostly due to reorientation of solvent molecules.

*Time-zero estimation*²¹ This model assumes that polar absorption spectra are inhomogeneously broadened due to the distribution of molecules over a range of local solvation environments and that the absorption spectra of two molecules residing in different microenvironments only differ by a frequency shift δ . The homogenous broadening in a polar solvent is assumed to be the same as in a nonpolar solvent. The frequency absorption spectrum in a polar solvent, $A_p(v)$, is thus given by the convolution of the absorption spectrum in a nonpolar solvent, $A_{np}(v)$, with the distribution of spectral shifts, $p(\delta)$,

$$A_p(\nu) \propto \int A_{np}(\nu - \delta)p(\delta)d\delta. \quad (2.9.3)$$

The distribution of spectral shifts, $p(\delta)$, is assumed to be Gaussian, *i.e.*

$$p(\delta) = \frac{1}{\sqrt{2\pi\sigma^2}} \exp\left[-\frac{(\delta-\delta_0)^2}{2\sigma^2}\right]. \quad (2.9.4)$$

Here σ denotes the variance of the distribution, and δ_0 is the average shift induced by the polar solvent. Provided that the shape of the absorption spectra in the polar and nonpolar solvent is known, the coefficients σ and δ_0 can be determined by using an iterative procedure.

Similar to Eq. 2.9.3, the desired fluorescence spectrum $S_p(\nu, \nu_{ex}, t = 0)$ can be expressed by

$$S_p(\nu, \nu_{ex}, t = 0) \propto \int A_{np}(\nu_{ex} - \delta)p(\delta)S_{np}(\nu - \delta)d\delta. \quad (2.9.5)$$

where $S_{np}(\nu)$ denotes the emission spectrum of the fluorophore in a nonpolar solvent. The emission spectrum at time zero can thus be reconstructed from the emission and absorption spectra in a nonpolar solvent and the absorption spectrum in a polar medium. However, the limited solubility of some probes in the nonpolar solvent can complicate the utilization of this method.

A simplification of Eq. 2.9.5 is possible for an excitation close to the absorption peak where almost no preferential selection of the solvation state occurs. The simplified equation is given by

$$\nu_p(t = 0) \approx \nu_p(\text{abs}) - \nu_{np}(\text{abs}) + \nu_{np}(\text{em}). \quad (2.9.6)$$

Here, ν denotes the peak positions of the maximum and the subscripts p and np indicate polar or nonpolar medium, respectively. From using this equation it follows that deviations in determining the position of the peak maximum do not exceed 50 cm⁻¹.²¹

2.10 Fluorescence correlation spectroscopy (FCS)

In FCS,²²⁻²⁴ one monitors intensity fluctuations $I(t)$ originating from a small illuminated volume. The fluctuations are caused by Brownian motions of fluorescent molecules entering and leaving the focal volume. The autocorrelation of these fluctuations is described by

$$g^{\text{FCS}}(t_1) = \frac{\langle I(t)I(t+t_1) \rangle}{\langle I(t) \rangle^2}. \quad (2.10.1)$$

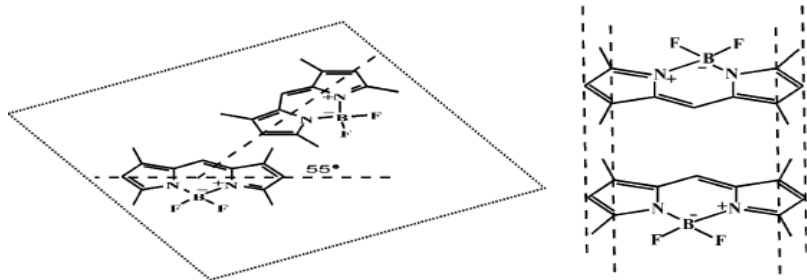
Here, $g^{\text{FCS}}(t)$ is an autocorrelation function. For 3D translational diffusion $g^{\text{FCS}}(t)$ is given by²³

$$g^{\text{FCS}}(t) = 1 + \frac{1}{1 + \frac{t}{\tau} \sqrt{\frac{t}{P_s^2 \tau_{\text{Diff}}}}} \frac{g^T(\phi, \tau_t)}{N_p}. \quad (2.10.2)$$

Here, N_p is the particle number, which expresses the number of fluorophores present in the illuminated focal volume, $P_s = b/a$ is the structure parameter, where b and a are the long and short axes of the 3D Gaussian focal volume (V_f). The diffusion correlation time (τ_{Diff}) is related to the diffusion constant $D = a^2/4\tau_D$, and finally g^T accounts for the intersystem crossing to the triplet state.

2.11 Suitable fluorescence probes for FRET/DDEM/SR experiments

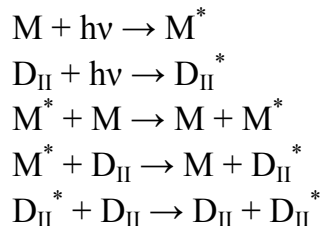
FRET/DDEM experiments. In order to have an efficient DA/DD pair, the donor emission spectrum should effectively overlap with the acceptor emission spectrum. While this is easy to accomplish for a DA pair it is more difficult for a DD pair, where the spectra belonging to the same molecule must overlap. In present studies BODIPY dyes have been used for several reasons: i) the absorption and fluorescence spectra as well as the fluorescence lifetime are insensitive to pH, polarity and viscosity; ii) they exhibit high values of the excitation coefficient; iii) they are stable even exposed to the illumination of intense lasers and iv) they form efficient DD-pairs with $R_0 \approx 57 \text{ \AA}$.²⁵



Picture 2.11.1: The proposed structures of dimers D_I (right) and D_{II} (left). The calculated centre of mass distance between the BODIPY:s in D_{II} is 3.8 \AA , and the angle between the electronic $S_0 \rightarrow S_1$ transition dipoles (dashed lines) is 55° .

It is less known that BODIPY can form dimers, which may influence the photophysics of the BODIPY monomer.^{26, 27} The so-called D_I dimers were observed only when two BODIPY monomers had been attached to the same molecule, not far away from each other. D_I dimers do not exhibit fluorescence and their absorption spectrum is slightly blue-shifted with the peak maximum at 477 nm. Experiments carried out by Mikhalyov et al.²⁷ suggest that the structure of D_I is compatible with that displayed in Picture 2.11.1 with almost parallel $S_0 \leftrightarrow S_1$ transition dipoles moments. The structure

of so called D_{II} dimers (Picture 2.11.1) is different. The dimer forms spontaneously when BODIPY molecules are solubilised at sufficiently high concentration in lipid bilayers. Under certain conditions, evidence for D_{II} dimer formation exists even at relatively low probe to lipid ratios (1:1000). The D_{II} absorption spectrum is red-shifted with the peak maximum centred at 580 nm. In contrast to D_I dimers, D_{II} dimers also fluoresce with a broad emission maximum at 630 nm. One has to consider the following processes when exciting BODIPY in lipid vesicles:



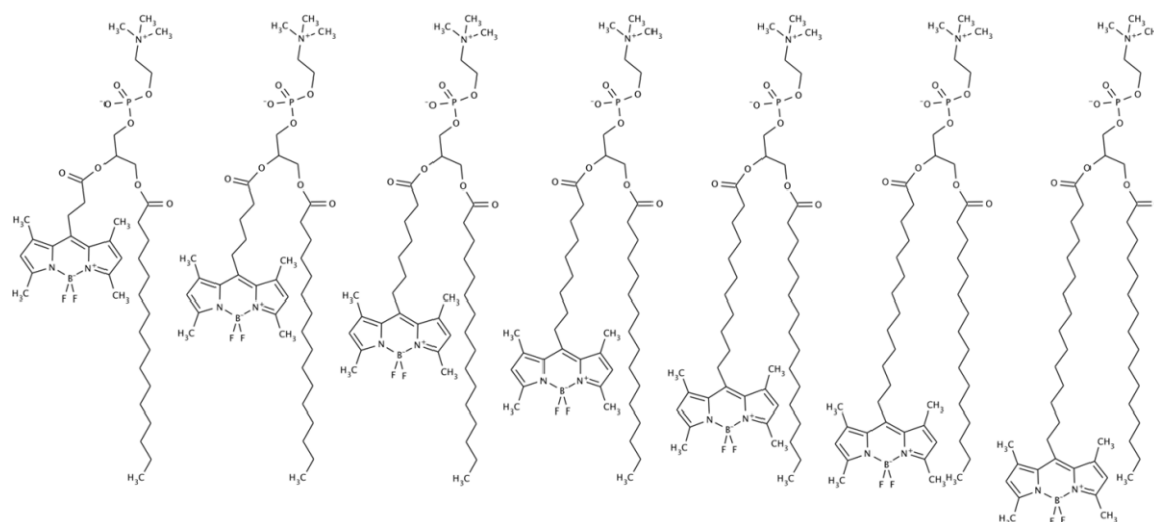
SR experiments. Fluorescent probes that are suitable for solvent relaxation measurements exhibit a huge change in the dipole moment after excitation. The surrounding water molecules react upon this sudden change by relaxing into a new energetically more favourable equilibrium state. Consequently, the evolution of time-resolved fluorescence spectra will depend on the viscosity and polarity of the solvent. In the case of PRODAN and LAURDAN the huge dipole moment change is stirred by the dialkylamino group attached to one side of the naphthalene ring, which works as the donor of electrons, and a carbonyl group attached to the other side of the ring, which works as the electron-acceptor. The relatively large Stokes shift is attributed to the charge transfer and to specific solute-solvent interactions.²⁸ The fluorescence lifetime of the probes should be long enough to enable observation of a substantial part of the solvent relaxation process.

3. RESULTS AND DISCUSSION

3.1 The localisation of fluorescent probes

3.1.1 Do methylated-BODIPY groups when attached at the end of long acyl chains loop back to the lipid-water interface (paper III)?

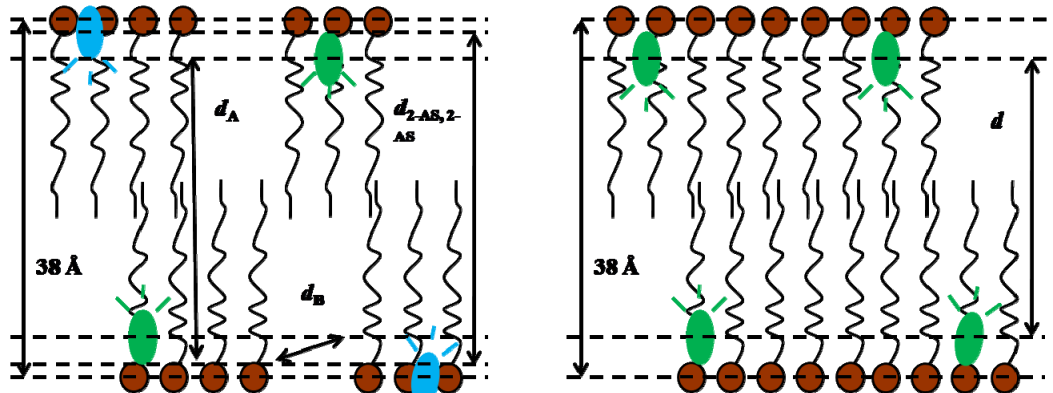
Motivations. There has been a lot of effort in localising various kinds of molecules in lipid membranes.²⁹⁻³² Some of these methods are based on fluorescence, *e.g.* the fluorescence quenching by free iodide.³³ However, this method assumes a known iodide concentration profile within the lipid bilayer, which is difficult to establish.³⁴ Another elaborate method, which is called parallax quenching,³⁵ relies on labelling the lipid acyl chains with a quencher at two different positions, and on the calculation of the relative positions between the molecule being localised and the two quenchers. Obviously, this method requires *a priori* knowledge about the position of the two quenchers. Paper III demonstrates a new approach which is based on energy transfer/migration, which enables precise measurement of the transversal distances of the probe inside lipid bilayers.



Picture. 3.1.1: The chemical structures of 1-palmitoyl-2-[Me₄-BODIPY-8)-acyl]-sn-glycero-3-phosphocholine with acyl containing 3-15 carbons.

This technique was applied to localise the popular BODIPY chromophore in DOPC bilayers. This could be helpful in future FRET studies, where one utilizes the newly found BODIPY position to localise another molecule. Interestingly, BODIPY attached to differently long acyl chains loops back to the lipid-water interface and is not preferentially localised at depths corresponding to the length of the acyl chain.³¹ In this study we tried to suppress the tendency of looping back by increasing hydrophobicity of the BODIPY ring. This was achieved by methylating the ring in the positions 1, 3, 5, 7. The newly designed probes (BnPC, where *n* denotes the number of

carbons) thus consisted of the methylated BODIPY chromophore attached to the *sn*-2 acyl chain with 3-15 carbons of the palmitoyl phosphatidylcholin molecule (Picture 3.1.1).



Picture. 3.1.2: (left) Interlayer energy transfer from the donors (2-AS) to the acceptor groups $\text{Me}_4\text{-BODIPY}$ which are linked to the BnPC:s . DAET is considered to take place from both 2-AC planes to $\text{Me}_4\text{-BODIPY}$ chromophores, where the distance between the two planes containing the donor 9-anthroyloxy groups $d_{2\text{-AS}, 2\text{-AS}} = d_A + d_B$. (right) DDEM among $\text{Me}_4\text{-BODIPY}$ groups in BnPC , localised in two planes separated by the distance d .

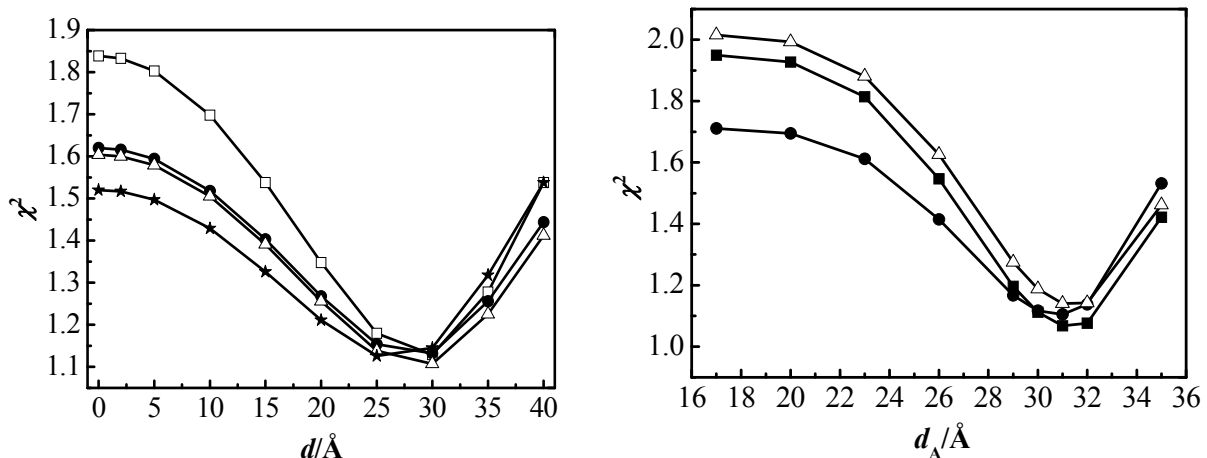


Fig. 3.1.1: (left) Chi-square values obtained when fitting the B-F model to experimental depolarisation decay curves. The studied molecules are B3PC (empty squares), B9PC (filled circles), B13PC (empty triangles), B15PC (filled stars) solubilised in DOPC vesicles. (right) Statistical best fit parameter chi-square values obtained when fitting the B-F model to TRFM experimental data. The chi-values correspond to fittings where the distance d_A has been used as a fixed parameter. The experimental data was measured for B3PC (filled squares), B9PC (filled circles), B15PC (empty triangles) in DOPC vesicles at 290.2 K.

DDEM experiments. Here the donors are assumed to be distributed in two parallel planes separated with a distance d . Depolarization experiments were carried out in order to monitor energy migration among donors. The analysis of data was based on fitting the depolarisation data to Eq. 2.7.1, with two adjustable parameters d and C_2 . The reorientation dynamics [$r_{\text{rot}}(t)$] was determined at a very low probe to lipid ratio (1:4000), where DDEM is practically non-existent. In contrast, depolarization experiments depending on DDEM were performed at a probe to lipid ratio of 1:200, where the sensitivity of FRET to d was satisfying. The electronic energy can migrate either to a donor localised in the same leaflet or to a donor positioned in the opposite leaflet (Picture 3.1.2). Therefore, G_{tot} is given by $G_{\text{tot}} = G_{\text{intra}}G_{\text{inter}}$. Irrespective of the length of the *sn*-2 acyl chain, the analysis of the depolarization data showed one pronounced chi-square minimum for $d = 27 \text{ \AA}$. Furthermore, Fig.3.1.1 reveals that the minima are deeper the shorter the *sn*-2 acyl chain is. This indicates that the Me₄-BODIPY group loops back towards the interface and that longer chains are more spread out due to entropy.

FRET experiments. Here 2-(9-anthroyloxy)-stearic acid (2-AS) was chosen as the donor because a) the anthroyloxy chromophore is due to the short acyl chain well localized at the lipid-water interface,^{36, 37} b) R_0 (2-AS/Me₄-BODIPY) = 42 Å is similar to the bilayer thickness. Two energy transfer processes were considered: 1) the inter-FRET from donors localized in one plane to the plane of acceptors localized in the same leaflet at the distance d_B 2) energy transfer to the opposite leaflet at the distance d_A (Picture 3.1.2). Consequently, the distance between the two donor planes is given by $d_{2\text{-AS},2\text{AS}} = d_A + d_B$. The optimal acceptor to lipid ratio was determined by simulations and found to be 1:200. The analysis was based on fitting time-resolved fluorescence data to Eq. 2.5.1. Since $d_B = d_A - d$, the number of fitting parameters is reduced to d_A and C_2 , where d denotes the distance between the Me₄-BODIPY planes and was estimated from DDEM experiments. The obtained value of $d_A = 31 \text{ \AA}$ was independent of the length of the *sn*-2 acyl chain (n). In addition, the chi-square minimum reached the lowest value for the shortest chain and was highest for the longest chain, which repeatedly suggests that the chromophore in B₁₅PC has more spatial freedom than that in B₃PC.

The order parameter profile determined by means of H²-NMR spectroscopy by selectively labelling different carbon atoms of the *sn*-2 acyl chain (each of them sensing different depths of the lipid bilayer) exhibits the following tendency:³⁸ regardless of the sharp dip at the carbon 2 it is constant within ca. 20% up to carbon 9 and then fast decreases to zero with increasing n . Fluorescence depolarisation experiments also enable measurements of the order parameter S_F by estimating the limiting anisotropy r_∞ of a reorienting dye

$$r_\infty = r_0 S_F^2 . \quad (3.1.1)$$

Table 3.1.1: The Me₄-BODIPY group's location in lipid bilayers of DOPC. The DAET and the DDEM were analysed by means of the B-F model. In the case of DAET, the longest distance between the plane of donors and the plane of acceptors is d_A whereas the shortest distance is d_B . In the case of DDEM, d describes the distances between two planes containing randomly distributed donors (Me₄-BODIPY). $C_{2,\text{exp}}$ and $C_{2,\text{calc}}$ correspond to reduced concentrations obtained from the data analysis and by calculations using the known acceptor concentration, respectively.

Donor	Acceptor	Donor:Lipid	Acceptor:Lipid	$C_{2,\text{exp}}$	$C_{2,\text{calc}}$	$d_A(\text{or})$	$d_B/\text{\AA}$
2-AS	B3-PC	1:100	1:100	0.73	1.05	31.4	3.6
2-AS	B7-PC	1:100	1:100	0.73	1.02	30.2	4.8
2-AS	B9-PC	1:100	1:100	0.73	0.95	30.8	4.2
2-AS	B13-PC	1:100	1:100	0.73	1.03	30.9	4.1
2-AS	B15-PC	1:100	1:100	0.73	1.05	31.5	3.5
B3-PC	B3-PC	1:200	-	0.70	0.70	29.0	-
B9-PC	B9-PC	1:200	-	0.70	0.67	26.9	-
B13-PC	B13-PC	1:200	-	0.70	0.71	28.7	-
B15-PC	B15-PC	1:200	-	0.70	0.71	27.7	-

This allows for a comparison between S_F and S_{NMR} . The S_F values of Me₄-BODIPY in B_nPC probes show no strong decrease for higher values of n (Fig. 3.1.2). The finding of approximately the same value of S for $n = 5$ and 15 actually supports the conclusion of a similar localisation of Me₄-BODIPY irrespective of n . Logically, one could expect a constant order parameter profile for the same localisation of B_nPC probes. Minor deviations from a constant S_F value may be due to restrictions originating from the probe labelled acyl chain. Consequently, the probes reorient more freely with increasing acyl chain length.

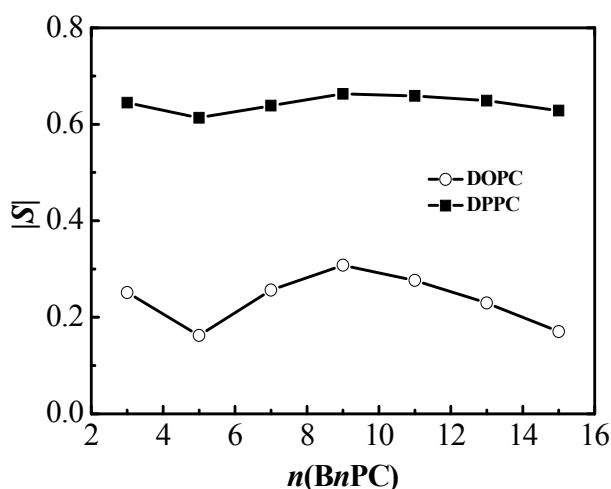
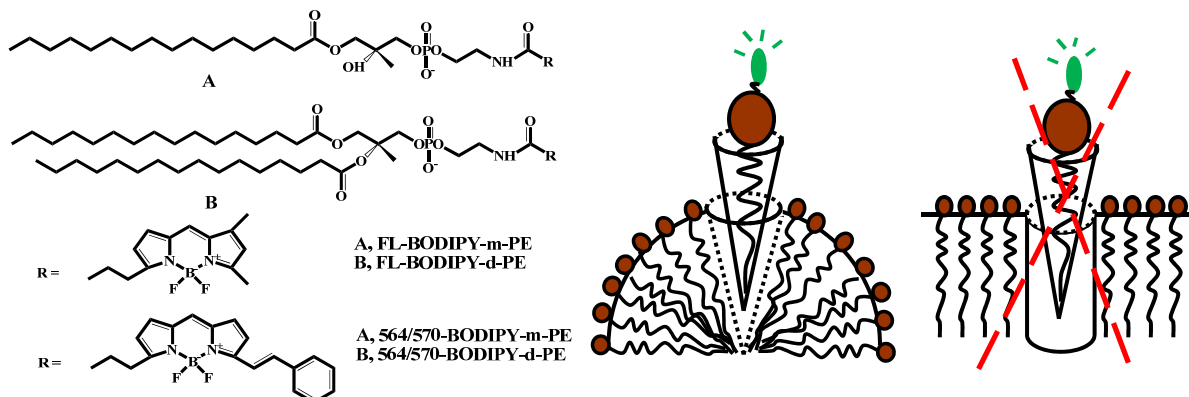


Fig. 3.1.2: The order parameter profile for the Me₄-BODIPY group in B_nPC ($n = 3, 5, 7, 9, 11, 13, 15$) solubilised in DOPC (empty circles) and DPPC (filled squares) vesicles at 290 K. The B_nPC to lipid ratio was 1:4000.

3.1.2 Do the conical like BODIPY probes preferentially locate in bilayers with high curvature (paper V)?

Motivations. The fact that lipid molecules self-assemble into structures with different curvature according to their molecular shape^{39, 40} has inspired us to investigate the affinity of cylindrically and conically shaped phosphatidylethanolamines to differently curved parts of lipid bilayers. One could hypothesize that a conical BODIPY head group labelled mono-acyl phosphatidylethanolamine would preferentially localise in regions with high curvature, such as toroidal pores formed by the peptide magainin-2 or at rims of lipid bicelles, whereas cylindrical BODIPY head group labelled diacyl-phosphatidylethanolamine would avoid the curved regions (*cf.* Picture 3.1.3). This would enable a preferential labelling of curved regions.

For this purpose, two differently shaped donor-acceptor pairs have been synthesized: 1) mono-acyl phosphatidylethanolamine (mPE) labelled with either FL-BODIPY (donor) or 564/575-BODIPY (acceptor) and 2) di-acyl phosphatidylethanolamine (dPE) labelled with the same dyes (Picture 3.1.3). The distribution behaviour was investigated by FRET experiments combined with MC simulations. The following systems which exhibited different curvature were studied: 1) large unilamellar vesicles with negligible curvature, 2) flat POPG bilayer containing highly curved toroidal pores⁴¹⁻⁴³ and 3) lipid bicelles comprising flat and curved regions.^{2, 3}



Picture 3.1.3: (left) Chemical structures of FL-BODIPY-mPE and FL-BODIPY-dPE (A), and 564/570-BODIPY-mPE and 564/570-dPE. (right) A cartoon displaying the preferred localisation of a conical-like probe, which prefers to be localised in curved regions (like rims of a bicelles, pores or as in this picture small micelles) over flat areas (such as large unilamellar vesicles).

Planar bilayers. Interestingly, mPE and to a less extent dPE probes exhibit a certain affinity to each other when solubilised in large DOPC vesicles. The rather modest clustering is supported by the following results: i) Analysis of time-resolved FRET

data by means of the B-F model yields 1.5-2x higher C_2 values than expected (based on lipid/probe mixing) and bilayer thicknesses d which are not physically relevant (*cf.* Tab. 1 and 2 in paper V). Since the FRET rate is faster for mPE than for dPE probes the former probes seem to cluster at a larger extent (Fig. 3.1.3). This could be explained by a more efficient hydrophobic stabilisation of the two acyl chains of the dPE molecule as compared to a single acyl chain of the mPE probe in the DOPC bilayer. ii) The time-resolved decays of all four probes in the absence of any acceptor become faster with increasing probe to lipid ratio, which is compatible with the formation of dimers (*cf.* Fig. 3-5 in paper V). In agreement with i), the decay is faster for mPE than for dPE due to the same reason. At the 1:50 ratios, dimers are visible even in the steady-state spectra (Fig. 5 in paper V).

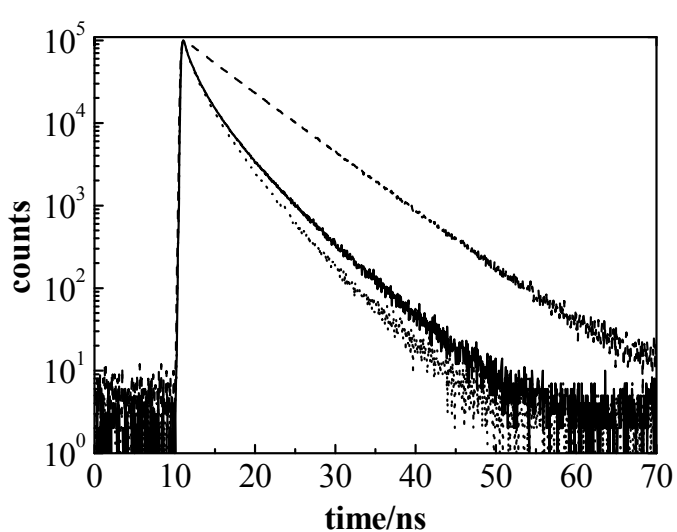


Fig. 3.1.3: TRF decays of donors at the donor to lipid ratio of 1:200 in DOPC vesicles at 20°C (downwards): donor mPE-BODIPY-FL in the absence of any acceptor (dashed), donor's fluorescence in the presence of the acceptor dPE-564/570-BODIPY 1:200 (solid line), and in the presence of mPE-564/570-BODIPY 1:200 (dotted line).

Bilayers containing torroidal pores can be prepared by adding the antibacterial peptide magainin-2 at ratios of 1:500 or higher to POPG bilayers.⁴¹⁻⁴³ Since there is no analytical model available accounting for FRET in a bilayer containing pores, Monte Carlo (MC) simulations have been carried out. The MC simulations can predict under what conditions FRET experiments are sensitive to probe localisation in pore containing bilayers. For small pore sizes with radii around 30 Å, the shape of the pore could be approximated by a cylinder. Two important insights follow from the simulations: i) While at higher peptide to lipid ratios (1:50) FRET cannot distinguish between the probes localized in the planes ($K_d = 0$) or in the pores ($K_d = \infty$), the resolution is sufficient at the 1:200 ratio (Fig. 3.1.4). ii) FRET cannot distinguish between the probes localized outside of pores ($K_d = 0$), or when equally distributed between the pores and the remaining area ($K_d = 1$). This happens because the pores are small compared to R_0 and cannot consequently influence the energy transfer rate. Nevertheless, K_d estimation is possible in the 1- ∞ range.

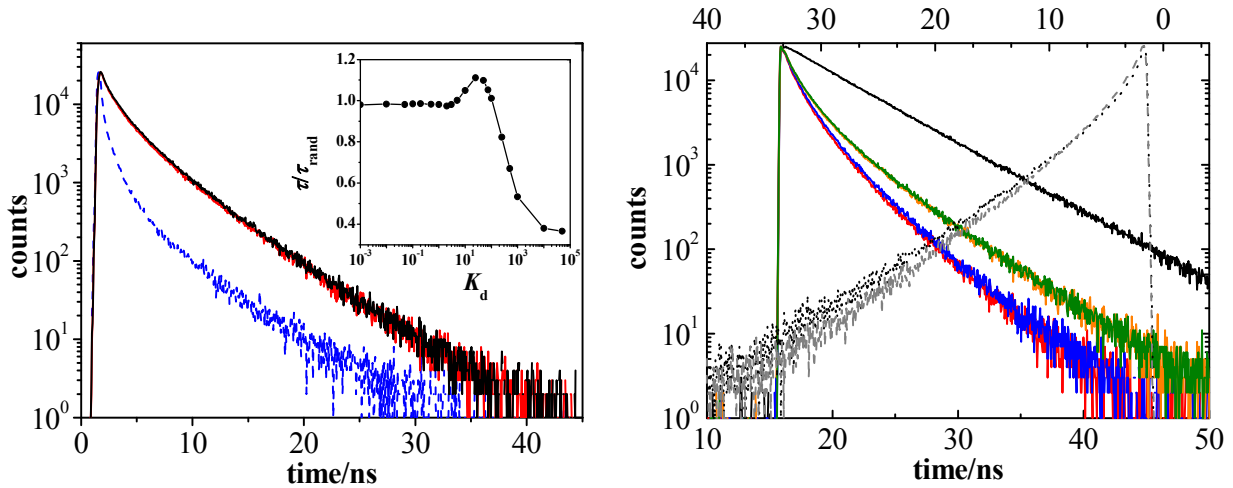
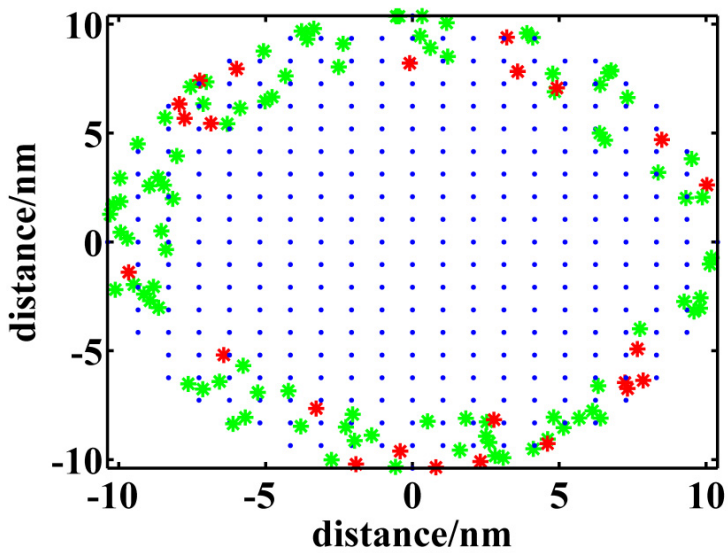


Fig. 3.1.4: (left) Generated TRF decay curves for energy transfer occurring in a POPG bilayer containing pores at the peptide to lipid ratios: 1:200. The distribution coefficient K_d was ∞ (blue), 0 (red) or 1 (black). Insert: The ratio between the average fluorescence lifetime and the average fluorescence lifetime if $K_d = 1$ as a function of the distribution coefficient K_d . (right, left y-axes) Decay curves are experimental for FRET occurring on a POPG bilayer with and without pores. The displayed decays illustrate the mPE DA pair before (red) and after addition of magainin-2 (blue), and the dPE DA pair before (green) and after addition of magainin-2 (orange). Decay for the mPE probe when no FRET occurs is also displayed (black); (right y-axes) Fluorescence decays are generated if $K_d = 1$ (dotted) and $K_d = 25$ (dashed line).



Picture 3.1.4: The distribution of donors (green stars) and acceptors (red stars) that having affinity to the curved rims on a bicelle as determined by the blue dots. View from the top.

Since the time-resolved FRET experiments with mPE and dPE probes do not show any change before and after addition of the peptide in the range of peptide to lipid ratios 1:500 and 1:100 K_d for mPE probes must certainly be lower than 10 (*cf.* insert of Fig. 3.1.4). If $K_d = 25$ one would need to observe a very well detectable change in the decay after adding the peptide at sufficient concentrations as is shown in Fig. 3.1.4 (right). As in vesicles, the different FRET rate for mPE and dPE probes can be explained by increased mutual affinity of the mPE probes.

Bicelles. In this study bicelles were chosen because of their disc like structure built of flat regions and a positively curved rim. The examined bicelles had the average radius of 103 Å,^{2, 3} and were prepared by mixing DPPC and DSPE-PEG-2000 in the ratio 75:25 mol%. MC simulations confirm that FRET occurring among probes distributed over the bicellar surface is differently influenced by the probes' location in the planar region ($K_d = 0$), the rims ($K_d = \infty$) as well as over the entire bicellar surface ($K_d = 1$, *cf.* Fig. 3.1.5). The most rapid decay was obtained for $K_d = 0$ and the slowest for $K_d = \infty$. In agreement with the previous results the experimental decay curves for mPE and dPE overlap perfectly at the probe to lipid ratio of 1:200 (*cf.* Fig. 8 in paper V). We therefore conclude that mPE probes have a rather modest affinity to regions with non-zero curvature.

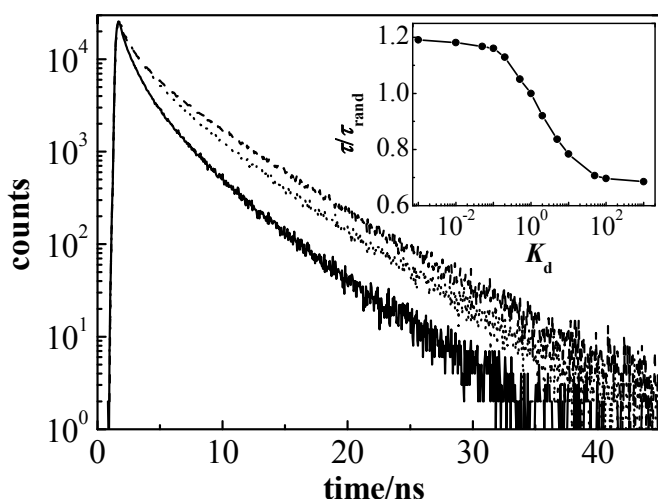
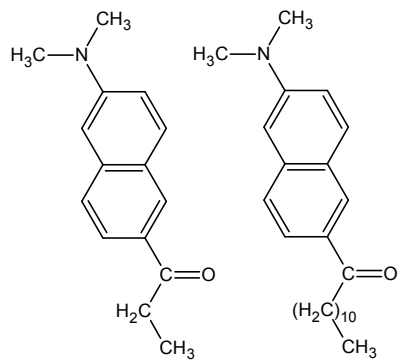


Fig. 3.1.5: Generated decay curves for FRET occurring on a bicelle. Donors and acceptors were distributed over the planes (solid), over the entire bicellar surface (dotted) or over the rims (dashed); (insert) The ratio between the average fluorescence lifetime and average fluorescence lifetime when $K_d = 1$ as a function of the distribution coefficient K_d .

3.1.3 Solvation dynamics of fluorescent probes PRODAN and LAURDAN in PCL-PEO vesicles (paper I)

Motivations. As it was mentioned in section 2.9, the relaxation of solvent molecules around an excited probe depends on the microviscosity and the polarity of their environment.¹¹ Since these physical properties exhibit a steep gradient within a bilayer the location of probes can be tracked by the SR technique.³⁶ In addition, one gains information about the dynamics of the SR process. It might be that solubilised dyes are

not localised at only one transversal distance from bilayer's center, but rather exhibit a complicated distribution profile within the bilayer. Then the time-resolved emission spectra (TRES) comprise a superposition of spectra. In this study we wanted to demonstrate that an analysis of TRES spectra is possible even when a dye is solubilized in two different environments. A careful analysis may then reveal where the dyes are localised, but also how the probe and the solvent molecules respond upon a sudden change of the electric dipole moment of the dyes.



Picture 3.1.5: Chemical structure of prodan (left) and laurdan (right).

The experiments have been carried out with biocompatible polystyrene-*block*-poly(ethylene oxide) vesicles dissolved in water and THF/water mixtures.⁴⁴ THF causes swelling of the PCL domain which in turn induces a relocation of the dyes

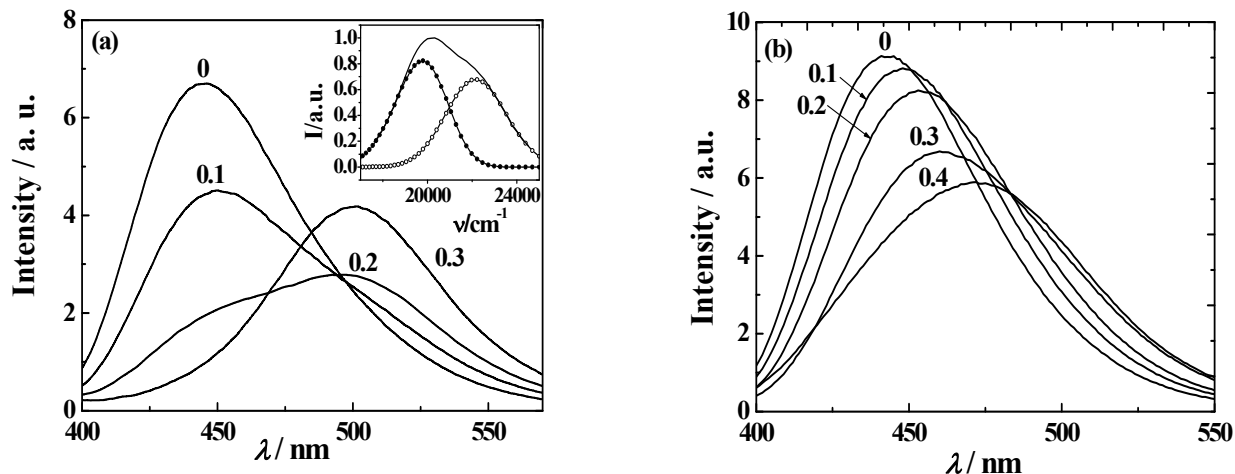


Fig. 3.1.6: Steady-state emission spectra of (a) prodan and (b) laurdan in the PCL-PEO/THF/water system. Volume fractions of THF in the water/THF mixed solvent are given at the corresponding spectra. Insert: Decomposed steady-state spectra of prodan imbedded in vesicles in 20 vol% THF/water mixture. The left and right spectra belong to prodan localized in the PCL hydrophobic domain and in the bulk solution, respectively.

solubilised in the vesicles. Prodan^{28, 45} and laurdane^{46, 47} dyes were used for the SR study. The same chromophore constitutes these probes, but laurdan contains an additional acyl chain (picture 3.1.5).

The steady-state fluorescence spectra of prodan and laurdan measured in a system composed of PCL-PEO vesicles and water are almost identical, but blue shifted as compared to that of prodan dissolved in water. Both chromophores are thus localised in the same environment (*i.e.* approximately at the same distance from the vesicle/water interface in a rather hydrophobic environment). Upon the addition of THF, the prodan spectra change to a much larger extent than those of laurdan (*cf.* Fig. 3.1.6) as a result of the probe's release into the bulk. Since prodan is lacking the acyl chain it is much easier released from the swollen PCL-PEO vesicles. Interestingly, the prodan spectra can be decomposed into two pertinent subspectra. The position and shape of the red shifted spectrum corresponds exactly to that of prodan dissolved in the particular THF/water mixture, whereas the blue-shifted spectrum belongs to prodan embedded in vesicles. The peak maximum of the latter spectrum is slightly red-shifted (450 nm) as compared to the aqueous solution (445 nm) due to swelling of the PCL domains.

Time-resolved fluorescence spectra can also be decomposed into two subspectra (Fig. 3.1.7): the blue-shifted subspectrum can be ascribed to the fraction of probes located close to the vesicle/water interface. The blue-shifted subspectrum moves towards longer wavelengths as the solvent relaxation proceeds, meanwhile the red-shifted spectrum belonging to probes dissolved in the bulk remains at the initial position, but shows a decreased intensity. This is because the relaxation of solvent molecules in the bulk is too fast to be captured by the used experimental apparatus. Therefore, decomposition enables separately measuring of SR dynamics for at least two probe populations localised in different environments.

A careful analysis of the obtained results also reveals that not only does the reorientation of solvent molecules contribute to the relaxation process but also the probe reorientation. The reasoning is as follows. First, chromophore groups of prodan and laurdan are located in the same region of the bilayer of the PCL-PEO/water system (see above). Second, the positions of both chromophores must be the same even in the PCL-PEO/water/THF 10 vol% system, since the first recorded TRES (*i.e.* spectra approaching the most the time zero) for both probes are very similar. Third, the correlation functions of prodan always decay faster than those for laurdan. But because the chromophores' environment is the same, the difference between the $C(t)$ functions for prodan and laurdan can only be explained by a faster reorientation of prodan in PCL-PEO vesicles, whose rotations/translations are not hindered by the long acyl chain.

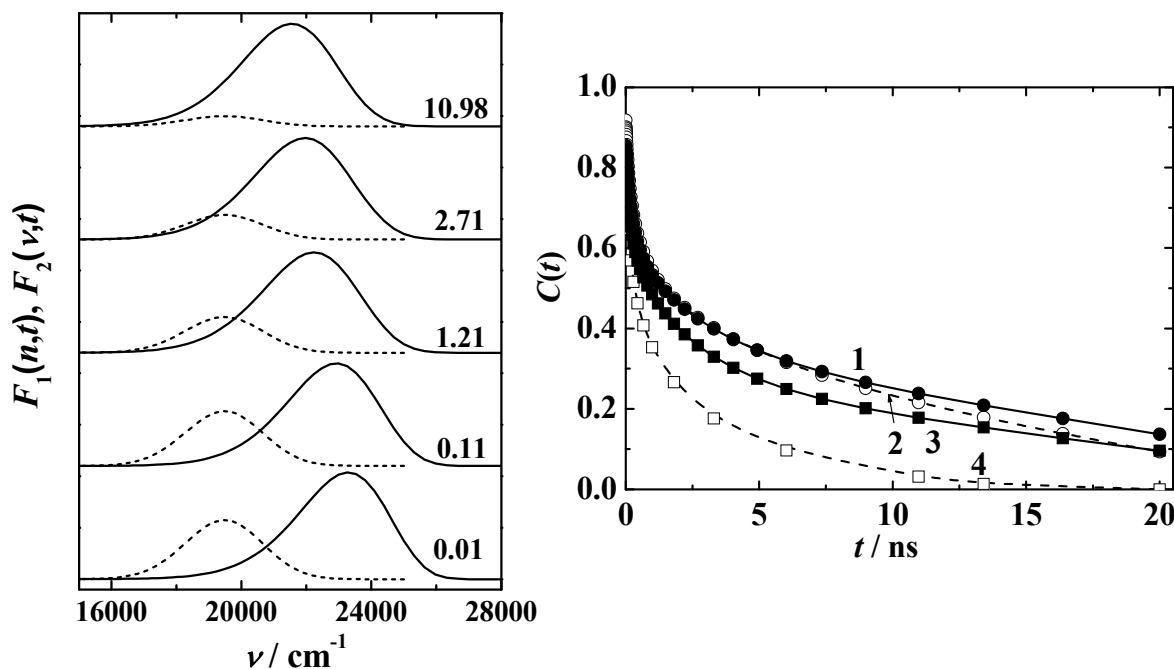
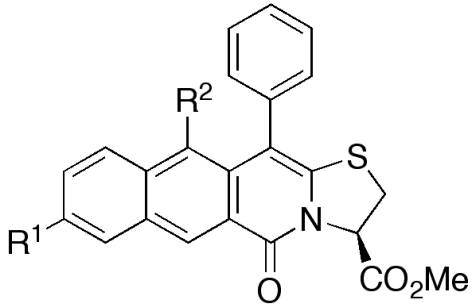


Fig. 3.1.7: (left) Decomposed time-resolved subspectra for prodan in PCL-PEO/water/THF(10%). The number at each spectrum indicates the time after excitation (in ns); (right) Correlation functions, $C(t)$, of the blue-shifted subspectra for laurdan (solid) and prodan (dashed) in the PCL-PEO/water system (curves 1 and 2) and in the PCL-PEO/water/THF(10 vol.%) system (curves 3 and 4), respectively.

3.1.4 Localisation of 2-pyridones in G_{M1} micelles (paper IV)

Motivations. The release of drugs from micelles but also loading efficiency are stirred by where the drug is localised.^{48, 49} For instance, a drug which resides in the micellar core is released into the bulk much slower than from the shell and the loading efficiency is restricted by the small micellar core. This is why the localisation of multi-ring fused 2-pyridones has been investigated. These compounds belong to the class of pyridones usually exhibiting interesting biological activity, including antitumor and antibacterial properties.⁵⁰⁻⁵³ The location in G_{M1} micelles was investigated for several reasons: i) the micelles are easy to prepare, ii) they exhibit narrow size distribution with a known aggregation number⁵⁴ and iii) specifically labelled gangliosides are available, which form a suitable DA pair with 2-pyridones. The intention was mainly to confirm or exclude compounds' localisation either in the core, at the core/shell interface or in the shell. A simple FRET approach was used, which is based on steady-state fluorescence experiments and data analysis by means of a simplistic model accounting for FRET within a micelle. Three pyridones derivatives have been positioned (Picture 3.1.6).



D-H: $R^1 = H; R^2 = H$

D-Me: $R^1 = H; R^2 = Me$

D-F: $R^1 = F; R^2 = H$

Picture. 3.1.6: The structures of the studied multi-ring-fused 2-pyridones.

Model. Assume that the donors are randomly distributed at the distance R_D from the micellar core, whereas acceptors are localised at the distance R_A from the micellar centre. Then the average energy transfer rate on a micelle is given by the distribution of distances between donors and acceptors according to

$$\omega = \frac{R_0^6 N_{Ac}}{\tau_D} \int_{R_{|R_D-R_A|}}^{R_D+R_A} \frac{P(R)dR}{R^6}, \quad (3.1.2)$$

where N_{Ac} denotes the number of acceptors, τ_D lifetime of the donor and $P(R)$ the normalised number density of acceptors at the distance R from a donor and is given by $P(R) = R/(2R_A R_D)$.⁵⁵ Integration of Eq. 3.1.2 yields

$$\omega \sim N_{Ac} \frac{R_A^2 + R_D^2}{(R_A^2 - R_D^2)^4}. \quad (3.1.3)$$

The randomly distributed acceptors surrounding the micellar centre can be considered as one effective quencher, which quenches the donor fluorescence at the rate ω . The ratio between the fluorescence intensity of the donor in the absence (F_D^0) and presence (F_D) of acceptors is then related to the total energy transfer rate according to:¹¹

$$\frac{F_D^0}{F_D} - 1 = \omega \tau_D. \quad (3.1.4)$$

Experimental results. Provided that 2-pyridones with unknown position in G_{M1} micelles work as donors localisation of acceptors (R_A) must be known a priori. In this study we have used G_{M1} gangliosides labelled in the polar (P) and nonpolar (NP) region by FL-BODIPY, whose position within the micelles was calculated by means of the assumption that the G_{M1} chain was fully extended. To avoid estimation of R_0 , τ_D and N_{Ac} we formed a ratio of Eq. 3.1.4 for the two different acceptors (FL-BODIPY-NP, FL-BODIPY-P). The experiments thus involved measurements of F_D^0 and F_D in the presence of either FL-BODIPY-NP or FL-BODIPY-P. The analysis concerns finding the minimum of the following expression:

$$\left[\frac{F_D^0(NP) - F_D(NP)}{F_D^0(P) - F_D(P)} \left(\frac{F_D(P)}{F_D(NP)} \right) - \frac{\omega(NP)}{\omega(P)} \right]^2 = 0 . \quad (3.1.5)$$

The minimisation routine yielded one minimum $R_D = 33 \text{ \AA}$ (*cf.* Table 3.1.2) for all three derivatives in the physically relevant range of $R_D \in (0; 54) \text{ \AA}$, which is given by the micellar centre and the hydrodynamic radius of G_{M1} micelles. 2-Pyridones are thus located at the core/shell interface irrespective of the substituent R^1 or R^2 , respectively. Similar location was found for the solvent relaxation probe prodan in PCL-PEO vesicles (paper I) but also for BODIPY and NBD in lipid bilayers.^{30, 31} For a more elaborated discussion see paper IV.

Table 3.1.2: Positions of 2-pyridones in G_{M1} micelles.

Donor	Acceptor	$F_D(NP)/F_D(P)$	$R_A/\text{\AA}$	$R_D/\text{\AA}$
D-F	FL-NP	1.15	23	34
	FL-P		42	
D-H	FL-NP	1.06	23	33
	FL-P		42	
D-Me	FL-NP	1.07	23	33
	FL-P		42	

3.2 Lipid nanodomain size estimation

Lipids dispersed into water organize into lamellar or non-lamellar phases, the former ones being more common in biological systems. Lamellar phases are found in lipid bilayers and can be classified according to their translational and conformational order. Liquid-disordered phase (L_d) is similar to the fluid state, where the acyl chains are disordered and the lipid molecules diffuse across the bilayer relatively fast. On the other hand, lipid chains in the solid-ordered state (S_o) are extended and highly ordered and the diffusion coefficient is very low. Finally, liquid-ordered phase (L_o) has some properties common to L_d and some to S_o : it is characterized by high conformational order and the diffusion coefficient slightly lower as compared to the L_d phase.

At equilibrium several phases may coexist with each other. The phase separation is driven by the fact that interactions of two different lipids A and B are usually repulsive. Interestingly, attractive forces exist between cholesterol and sphingomyelin or between cholesterol and a saturated phosphatidylcholine,⁵⁶ which actually can explain accumulation of both lipids in the L_o domain phase. For a ternary mixture of DOPC/DPPC/cholesterol, the phase separation is explained by three pairs of binary interactions: i) the favourable interaction between cholesterol and ordered lipids and the unfavourable interactions of ii) ordered with disordered lipids and iii) cholesterol with the disordered lipids.^{57, 58}

Phase separation may lead to the formation of microscopic or even nanoscopic liquid-ordered lipid domains. Sometimes these domains are called rafts and are connected with several functional roles such as signalling, membrane trafficking or viral infection. The domains tend to adopt a circular shape in order to minimize the line tension originating from the height mismatch between the L_o and L_d phases and the steric interactions at the phase interface.⁵⁹ As the domains become larger their morphology changes from the flat one to a dimpled one, the latter one facilitating repulsive elastic interaction of the coalescing domains. Consequently, separated small domains cannot merge into one large domain as a result of minimization of the line tension.⁶⁰

In order to observe the phase behaviour of lipid system one can use electronic energy transfer approach. Actually, despite the advances in far-field optical microscopy⁶¹ FRET still remains the most powerful technique in lipid nanodomain size estimation.

3.2.1 What are the limitations of FRET in estimations of lipid nanodomain sizes (paper VI)?

Motivations. The estimation of lipid nanodomain sizes by FRET is based on measuring energy transfer efficiency between donors and acceptors that have increased affinity either to the L_o domain phase or to the remaining L_d phase. As will be shown resolution of FRET is ruled by affinity of probes to the particular phase. Therefore, the localisation of probes within a bilayer influences the sensitivity of FRET and as a thumb of rule the resolution increases with increasing affinity of probes to L_o/L_d phases. It seems that possible impact of the affinity of probes on the resolution is in general underestimated. Concerning the availability of suitable probes, dyes exhibiting substantial affinity to the L_o phase are still missing.⁷ Assuming realistic distribution coefficients we explored theoretical limits of FRET in nanodomain size estimation by applying MC simulations.

Table 3.2.1: Conditions that have been used in order to discuss FRET limits in the nanodomain size estimation. F and F_{uni} denote steady state intensities for uniform and nonuniform distribution of probes, respectively.

Conditions	TRFM	Steady-state range	Colour
1.	Domains are beyond the resolution	$F/F_{uni} < 1.05$	Red
2.	Domains are close to the resolution	$1.05 < F/F_{uni} < 1.1$	Orange
3.	Domains are detectable	$1.1 < F/F_{uni} < 1.2$	Yellow
4.	Domains are safely resolvable	$F/F_{uni} > 1.2$	Green

Three situations may arise when distributing D/A molecules in a bilayer 1) D:s/A:s reside inside L_o domains, 2) D:s/A:s are excluded from these, and 3) D:s/A:s exhibit

increased affinity to different phases. Concerning the limits four conditions are considered (*cf.* Fig. 3.2.1 & Tab.3.2.1). Below most important outcomes of the simulations will be summarized. More elaborate discussion can be then found in paper VI.

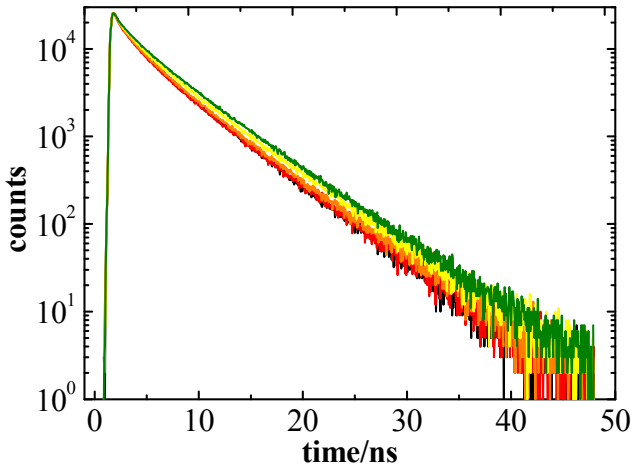


Fig.3.2.1: Fluorescence decays generated for the uniform distribution of D/A (black), and those corresponding to the following conditions (cond.): cond. 1 (red), cond. 2 (orange), cond. 3 (yellow) and cond. 4 (green). The radius of domains $R = 10$ nm and the domain area ranged from 4 to 34 %.

Case I. The favourable 4th condition is reached when K_D and $K_A > 10$ (Fig. 3.2.2). Here, K_D and K_A denote distribution constants of D/A defined by $K_i = [i]_{Lo}/[i]_{Ld}$. Unfortunately, such probes are not yet available. For more realistic values of K_D and $K_A = 3$ domains with an area exceeding 20 % and radii $> 1.6R_0$ might be resolved by TR FRET (cond. 2), whereas for $K_D = 5$ and $K_A = 5$ (*i.e.* comparable to labelled cholera toxin) domains with an area > 15 % and radii $> 1R_0$ can be detected by TR FRET (cond. 3 and 4). This setup is not realistic for determining sizes < 20 nm with up to now available probes.

Case II. As can be seen from Fig. 3.2.2 this setup is not favourable for determination of raft sizes around R_0 . For instance, probes with rather high affinity to L_d ($K_D = K_A = 0.01$) can only resolve domains with sizes > 20 % and radii $> 1.5R_0$. BODIPY-PC/fast-DiI DA pair has $K_D = K_A \approx 0.1$ and has been used for characterization of domains in DOPC/DSPC/Chol system.⁶ The authors speculated that the domains had radii in the range 2-8 nm. According to our study, domains with $R > 5$ nm and areas > 25 % could have been resolved. Although high L_d affinity probes exist they are not useful for detection of small domains < 20 nm.

Case III. Since probes with high affinity to the L_d phase already exist we used $K_A = 0.01$ in all simulations. The value of $K_D = 5$, comparable to cholera toxin, which has the highest K_D so far, is high enough to observe domains over a broad range of sizes, but still domains with area < 2.5 % and domains with radii $< 1R_0$ and occupying $< 10\%$ of the area are beyond the resolution. To observe the very small domains with $R < R_0$ and area of only few % $K_D = 40$ would be needed. Care should be taken when

interpreting data. For instance, Hammond et al⁵ used a favourite DA pair perylene and DiI ($K_A = 0.01$) to detect nanodomain formation by steady state measurements. Because they did not see any changes in the intensity before and after a hypothetical domain formation they concluded that no domains were formed. Based on the simulations and even by using an approximately four times higher K_D value than determined by us, formation of nanodomains < 20 nm cannot be excluded.

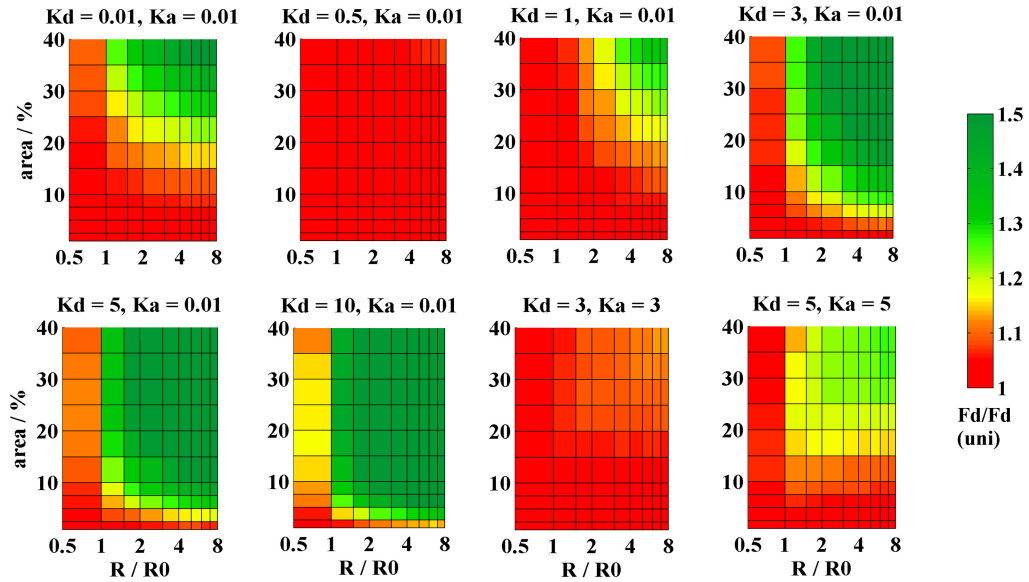


Fig. 3.2.2: The resolution of FRET represented by the intensity ratio of D:s (F_D) and D:s/A:s when D:s/A:s are distributed uniformly in the bilayer ($F_D(\text{uni})$) as a function of the domain area and the relative domain radius (divided by R_0). The D-lifetime was 6 ns in the L_o and L_d phase. The red corresponds to the condition (cond.) 1, the orange to the cond. 2, the yellow to the cond. 3 and the green to the cond. 4. For $[K_D = 0.01, K_A = 0.01]$, $[K_D = 3, K_A = 3]$ and $[K_D = 5, K_A = 5]$ the ratio $F_D(\text{uni})/F_D$ is displayed instead. Values above 1.5 are displayed with the same colour at the limiting value.

3.2.2 Is the formation of nanodomains proceeding microscopic phase separation (paper VII)?

Motivations. It has been demonstrated that cholera toxin induces in the presence of small amounts of ganglioside G_{M1} microscopic liquid ordered (L_o) and liquid disordered (L_d) phase separation both in giant unilamellar vesicles (GUVs) formed by lipid mixtures consisting of dioleoylphosphatidylcholine (DOPC), sphingomyelin (Sph) and cholesterol (Chol)⁵ as well as in plasma membrane spheres.⁶² Clustering of lipid components plays a crucial role in various membrane associated processes such as signalling of immune receptors.⁶³ One could speculate that formation of crosslinker-induced nano-scaled domains proceeds the microscopic phase separation (detectable by optical microscopy) along the trajectory displayed in Fig. 3.2.3 heading from the L_d

to the L_0 phase. To test this hypothesis two colour z-scan fluorescence correlation spectroscopy,⁶⁴ which enabled a dynamic characterization of nanodomains, and Förster resonance energy transfer combined with Monte Carlo simulations have been applied. The latter two techniques might reveal the size of the domains together with the area the domains occupied in the bilayer.

The performed experiments focused on characterization of bilayers with compositions close to the microscopic separation (points **B** and **C** in Fig. 3.2.3). At the point **A** the used bilayer did not contain any Sph and was homogenous (\approx without any domains), whereas at the points **D** and **E** phases there is a microscopical phase separation (cf. Fig. 3.2.3 and Tab. 3.2.2). Experiments have been performed at low and high loadings of CTxB (marked by a prim).

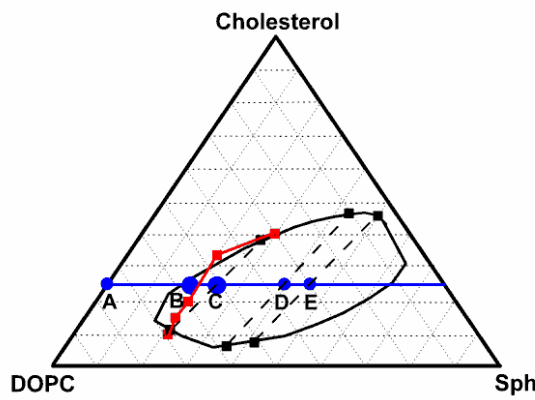


Fig. 3.2.3: A ternary phase diagram for DOPC/Sph/ Cholesterol lipid mixtures as given in literature: black curve and the tie-lines and the red curve were published by Smith *et al* and Farkas *et al*, respectively. The line connecting points **A** to **E** denotes compositions with constant cholesterol content. All measurements were performed at compositions given by the points **A** to **E**. These also correspond to the lipid compositions given in Table 3.2.2.

Table 3.2.2: Molar fractions of lipids in GUVs discussed in this manuscript.

	DOPC	Sph	Chol	DOPG	G_{M1}
A	0.68	0	0.25	0.05	0.02
B	0.49	0.19	0.25	0.05	0.02
C	0.44	0.24	0.25	0.05	0.02
D	0.29	0.39	0.25	0.05	0.02
E	0.23	0.45	0.25	0.05	0.02

Point A: At this composition the bilayer contained no Sph and was homogenous. The addition of CTxB in the amount corresponding to a high loading caused no changes in lipid dynamics, nor any structural phase changes.

Point B: The diffusion of CTxB labelled by Alexa 647 exhibits very distinct changes after the titration with additional crosslinker (**B** → **B'**). A substantially prolonged component in the autocorrelation fluorescence curve $g^{\text{FCS}}(t)$ appears for **B'** (Fig. 3.2.4), which could be a consequence of either a massive aggregation of CTxB molecules, or coalescence of condensed G_{M1} molecules around the crosslinker molecules. The mutual interaction of crosslinker molecules is excluded by the fact that no cross-correlation was detected between CTxB labelled by Alexa 488 or Alexa 647.

Interestingly, FRET detects inhomogeneities already in **B**, but these are smaller than in **B'**. The exact raft size was estimated by fitting the experimental decays to those generated by MC simulations. The number of fitting parameters involved the domain radius, R , and the area domains occupy in the bilayer, area (for details on MC simulations see supplementary material of the paper VI). As shown in Fig 3.2.5, the optimisation routine provides a pronounced minimum for **B** when $R = 5\text{-}5.4 \text{ nm}$ and $\text{area} = 6\text{-}9 \text{ \%}$, and for **B'** when $R = 8 \text{ nm}$ and $\text{area} = 6 \text{ \%}$.

Point C: FCS reveals diffusion obstacles for the composition **C**, but on the contrary to **B** the obstacles are present already at low loadings of CTxB and do not change by further titration with CTxB. The fitting of the FRET decays yielded an CTxB independent value of $R = 24 \text{ nm}$ and $\text{area} = 3 \text{ \%}$.

Table 3.2.3: Mean transition times of CTxB-647 through the illuminated spot - the minimum value obtained when membrane was centred in the beam waist. Stdev denotes the standard deviation of t_D and N gives number of z-scans acquired for the given composition.

	A	B – low load	B – medium load	B – high load	C – low load	C – medium load	C – high load	D	E
t_D/ms	6.6	5.9	40.3	46.5	12.8	14.6	12.0	7.1	22.1
Stdev/ms	0.08	0.21	2.24	10.54	0.92	2.86	6.82	0.66	4.99
N	4	4	2	3	2	3	3	3	4

An interesting piece of knowledge is obtained from the analysis of the minimum mean transition time t_D , *i.e.* the time a fluorescent molecule spends in the waist (the narrowest part) of the illuminated focal volume. The transition time is substantially longer in **B** and **C** than in **A**, which indicates heterogeneities in the bilayer. The value of t_D depends on the time the dye is confined in nanodomains, τ_{conf} , the time-based distribution coefficient α , and the effective diffusion coefficient D_{eff} according to $t_D \approx 2\alpha\tau_{\text{conf}} + \frac{\omega^2}{4D_{\text{eff}}}$,⁶⁵ where the confinement time τ_{conf} is ruled by the transition of the dye into and from the domains. Surprisingly, we obtained approximately 3 times

longer confinement time for **B** than for **C**, although the bilayer with the composition **C** contained larger domains. This finding indicates that the **C** domains are more permeable for CTxB than the smaller **B'** domains, *i.e.* CTxB binds more tightly to the **B'** domains. CTxB seems thus to be more substantial for the existence of the **B'** than the **C** domains, probably because it can compensate the lack of sphingomyelin in the **B'** domains. This would also explain why titration of GUV's with additional CTxB induced changes in the bilayer with **B** composition only.

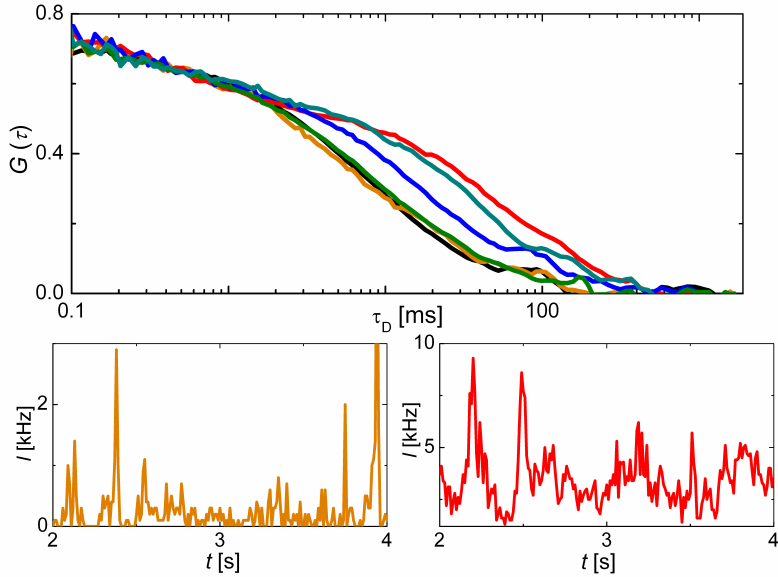


Fig. 3.2.4: Upper part: autocorrelation curves for CTxB-647 in upper GUV membrane centred in the waist of the focal spot at different lipid compositions: **A** (black), **B** – low load of CTxB-647 (orange), **B** – high load of CTxB-647 (red), **C** (blue), **D** (olive), **E** (dark cyan). Lower part: intensity traces for CTxB-647 in **B** composed membranes at low (orange) and high (red) load of CTxB-647.

With respect to the sizes of **B** domains, they can be formed only by a single pentameric unit, which is probably surrounded by the sphingomyelin enriched shell. A domain radius of 8 nm of **C** domains allows for the formation of a domain with a maximum of 2-3 pentameric units. It could be that the larger 8 nm domains are formed as a result of collisions between the pentameric units.

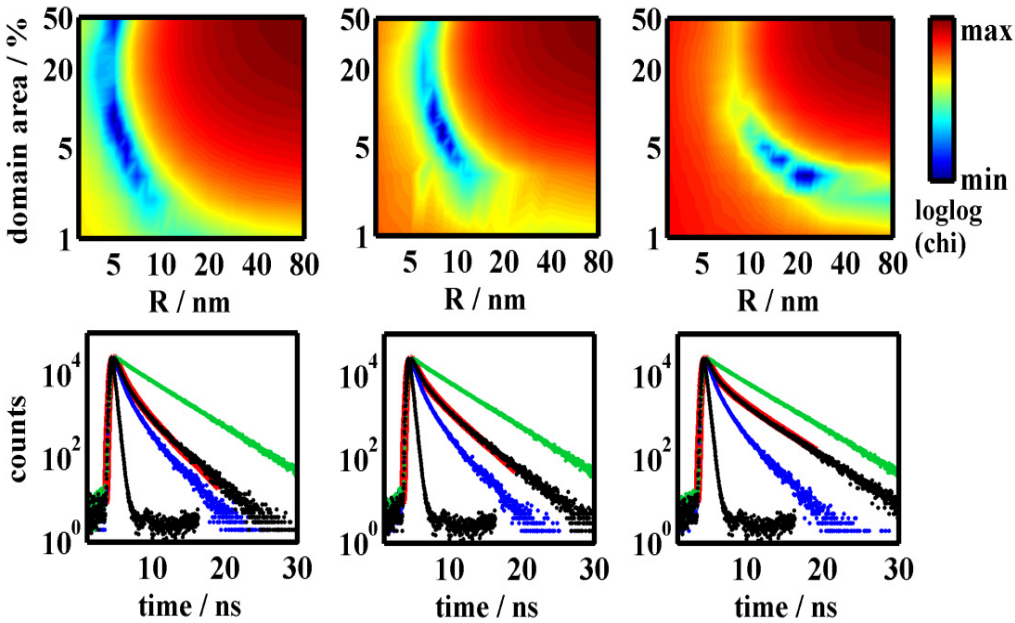


Figure 3.2.5: Upper part: Best fitting chi-square parameter as a function of the domain radius and the area domains occupy in the bilayer. A minimum is found at $R = 5$ nm and domain area 9 % for the composition **B** (on the left), $R = 8$ nm and domain area 6 % for the composition **B'** (in the middle) and at $R = 24$ nm and domain area 3 % for the composition **C** (on the right). Lower part: Displayed time resolved fluorescence decays of CTxB-488 serving as the donor (D) representing the bilayer containing (i) D only (green line); (ii) D and A distributed between domain and non-domain regions (black line) and (iii) D and A, where both D and A are uniformly distributed in the bilayer without any domains (blue line). The red line coinciding with the black line is the best fit calculated by means of MC simulations. Instrument response function is displayed too. Figures in the lower part correspond to those in the upper part.

3.2.3 Self-assembly of $\text{G}_{\text{M}1}$ ganglioside molecules in water (paper II)

Motivation (A). $\text{G}_{\text{M}1}$ molecules are known to prefer a detergent resistant liquid-ordered domain phase⁶⁶ and to self-aggregate in model lipid membranes.⁶⁷ When dissolved in water these lipids spontaneously form micelles over a broad range of concentrations. Upon heating, the micellar aggregation number, N_{agg} , starts to decrease, probably due to the molecular transition from one to another molecular conformation.^{68, 69} However, this explanation has not been supported by Orthaber and Glatter,⁷⁰ who explained the changes by the existence of larger aggregates, which are dissolved upon increasing the temperature. This controversy has inspired us to look on the self-assembling behaviour.

Motivation (B). In order to measure N_{agg} one can apply fluorescence correlation spectroscopy (FCS). The correct estimation of N_{agg} relies on the preciseness with which the illuminated focal volume V_f is measured. The most rapid way how to determine V_f is to measure the diffusion time τ_{Diff} of a fluorescent dye with known diffusion coefficient across the focal volume. For this purpose, rhodamine 6G (R6G) is frequently used and the focal volume V_f is calculated from⁷¹

$$V_f = (4\pi\tau_{\text{Diff}}D_{\text{R6G}})^{3/2}P_s . \quad (3.2.1)$$

Here P_s is obtained by fitting the correlation function $g^{\text{FCS}}(t)$ by Eq. 2.10.2. Since it is experimentally difficult to measure the diffusion coefficient at low concentrations corresponding to the FCS level, a value $D_{\text{R6G}}(\text{old}) = 280 \text{ m}^2\text{s}^{-1}$, which was published 1974, was used for more than 30 years.²⁴ A recently published value $D_{\text{R6G}}(\text{new}) = 426 \text{ m}^2\text{s}^{-1}$ differs considerably from the previously established one. This implies that the so far calculated N_{agg} by means of FCS deviate 0.54 times from the true value.^{72, 73}

Therefore *the goal* of this study was two-fold: (1) to reinvestigate the controversial temperature behaviour by light scattering and FRET, and (2) once the correct aggregation numbers of G_{M1} micelles were known to use them in order to test the recently published reference values of rhodamine-6G diffusion coefficient needed for the estimation of N_{agg} .

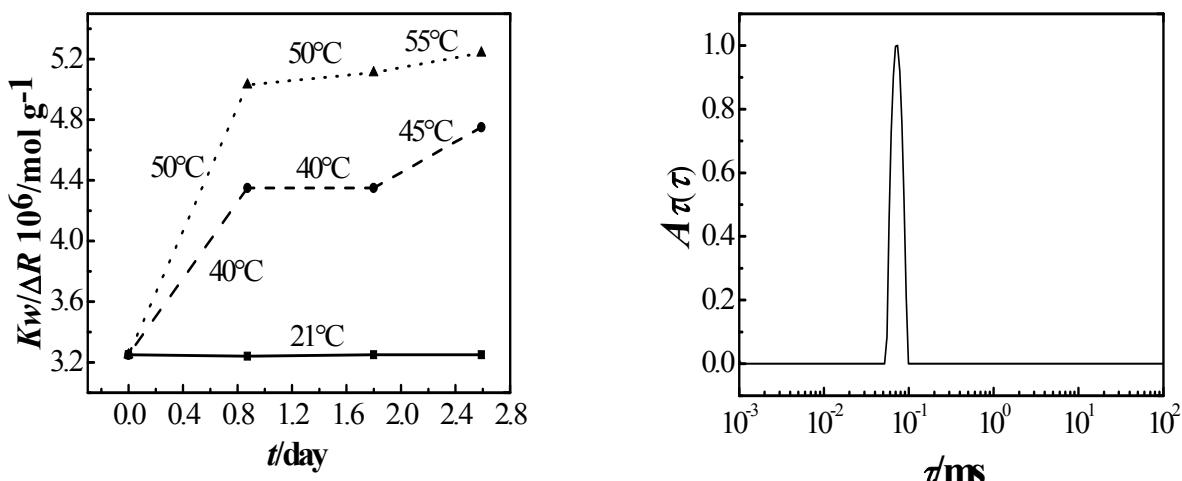


Figure 3.2.6: (left) $K_w/\Delta R$ proportional to $1/M_w^{\text{app}}$, where M_w^{app} is the apparent molar mass of G_{M1} micelles, at different heating cycles (see the text). Solid line: reference sample with no heating, dashed line: heating up to 40°C until the sample is equilibrated and then up to 45°C , solid line: heating up to 50°C until the sample is equilibrated and then up to 55°C ; (right) Dynamic light scattering relaxation time distributions (measured at the scattering angle 90° and at the temperature 21°C) of G_{M1} micelles.

(A) *The temperature behaviour.* Information about the system polydispersity is contained in the autocorrelation curves obtained from light scattering (LS). Distribution of relaxation times shows one narrow peak corresponding to the hydrodynamic radius $R_H = 5.4$ nm. The shape and position of the peak remains unchanged when measured before and after filtration. Interestingly, the aggregation number of G_{M1} micelles is really responding to elevated temperatures (Fig. 3.2.6 left). One finds that nothing happens with the micelles up to 30 °C, but then the aggregation number starts decreasing irreversibly. These results are in agreement with Cantu *et al* (and in contradiction with Orthaber and Glatter). The former group explained the changes by irreversible transitions from one to another energetically more favourable state. The extrapolation of LS data to zero concentration and zero scattering angle yielded that the mass-averaged $N_{\text{agg}} = 263 \pm 5$ at 21 °C.

On the contrary to LS, FRET and FCS provide number-averaged aggregation numbers, which are equal to or lower than the mass-averaged N_{agg} (due to polydispersity). FRET method involves labelling of micelles by donors and acceptors, where the latter act as fluorescence quenchers, and furthermore estimation of the fraction of micelles which do not contain any acceptor. This fraction is accessible by time-resolved fluorescence, and is by means of Poissonian distribution related to the average number of quenchers per micelle $\langle n \rangle$. The aggregation number is given by the final equation $N_{\text{agg}} = ([\text{Lipid}]\text{-cmc})\langle n \rangle / [\text{A}]$, where cmc is critical micellar concentration. By using three different DA pairs consistent results have been obtained over a broad concentration range $N_{\text{agg}}(\text{ET}) = 168 \pm 4$. This value has served us as the reference value in the calibration of the FCS method (part B).

(B) *FCS calibration.* The measurement is based on estimating the number of micelles (N_{mic}) within the illuminated focal volume V_f . Since only labelled micelles are observed by FCS each micelle contains at least one dye molecule in order to obtain the correct value of N_{mic} . To achieve this, one can titrate the micelles by a fluorescent dye that exhibits high affinity to the micelles, and to monitor the number of particles in the focal volume (one fitting parameter of $g^{\text{FCS}}(t)$) as a function of the dye concentration. When a plateau is reached, all micelles must be labelled (Fig. 6 in paper II). Similarly to FRET, the final N_{agg} is calculated as $N_{\text{agg}}(\text{FCS}) = ([\text{Lipid}]\text{-cmc}) / [\text{Mic}]$, where $[\text{Lipid}]$ is a priori known and $[\text{Mic}] = N_{\text{mic}} / V_f$. By using the recently published value of D_{R6G}^{73} one obtains aggregation numbers spread around the average value 168, obtained by FRET as well, while by using the old value²⁴ one would obtain the value of $N_{\text{agg}}(\text{FCS, old}) = 91$, which poorly agrees with $N_{\text{agg}}(\text{FRET})$.

4. CONCLUSIONS

The thesis emphasizes that electronic energy transfer is a powerful method in i) finding the equilibrium position of fluorescent probes in homogenous as well as inhomogenous lipid bilayers and ii) in measuring sizes of lipid domains, which are still beyond the resolution of a fluorescent microscope.

More specifically, localisation of the BODIPY chromophore methylated at the positions 1, 3, 5, 7 was studied when it was attached to the differently long *sn*-2 acyl chain of phosphatidylcholins (paper III). It has been shown that the Me₄-BODIPY chromophore loops back to the lipid-water interface and is not residing at depths corresponding to the acyl chain length. The transverse positioning of fluorescent probes is usually done when using less precise steady-state parallax quenching experiments. Here a FRET/DDEM method has been introduced instead. The analysis is based on fitting models to time-resolved fluorescence data (*i.e.* thousands of data points are accounted for in comparison to only one or a few points given by the steady-state intensity) to the analytical model describing energy transfer/migration between donors/acceptors in a lipid bilayer.

There exist analytical models which account for FRET in a limited number of cases. This limitation can be circumvented by making use of Monte Carlo simulations. In paper V we have used this approach to model FRET on bilayers containing highly curved toroidal pores and on bicellar surfaces comprising planar and curved regions. A comparison between modelled and experimental decay curves enabled exploring the affinity of conically and cylindrically shaped BODIPY labelled phosphoethanolamines to differently curved regions of the above mentioned systems. Surprisingly, the studied DA pairs showed a rather modest affinity to the antibacterial pores. Since this project aimed at developing probes with high affinity to the pores experiments are currently performed with more conical probes, which should increase the labelling efficiency of pores.

Rather simplified FRET models can provide useful information about the localisation of fluorescent probes as well. In paper IV a simplistic model was used which accounts for FRET between donors and acceptors found in a micelle at two distances from the micellar centre in order to localise three different derivates of 2-pyridones. Irrespective of whether the derivate was fluorinated, methylated or hydrogenated, respectively, it turned out that the dyes are solubilised at the core-shell interface of G_{M1} micelles. This finding is in agreement with the paper III, where the methylation of BODIPY at four positions did not influence localisation of the chromophore within the DOPC bilayer.

The location of probes in polymeric vesicles was determined by the solvent relaxation technique (paper I). Despite the FRET method the SR technique also provides information about the dynamics of solvent relaxation, which is connected to polarity and viscosity of the solvent. A comparison between solvent relaxation data obtained for PRODAN and LAURDAN in PCL-PEO vesicles suggests that a reorganisation of solvent molecules and polymer units around the dye, but also a lateral motion of the probe with respect to the vesicle contributes significantly to the relaxation process. Moreover, the study shows that the analysis of time-resolved emission from a probe distributed in two media is in principle possible.

Despite recent advances in the field of super resolution microscopy FRET still remains the most powerful method in the estimation of lipid nanodomain sizes. In paper VI theoretical limits of FRET during the measurement of lipid domain sizes were explored. It turned out that limitations of FRET are mainly caused by low affinity of probes to either the L_o or L_d phase. As the best approach appears the case when D:s/A:s prefer a different phase. Then a D/A pair with distribution constants $K_D = 5$ and $K_A = 0.01$ already resolves a broad range of domain sizes. However, only probes with high affinity to the L_o phase will enable detection of very small domains or domains occupying only few percent of the bilayer area. Situation when D:s/A:s prefer the same phase, either the L_d or L_o phase, is not yet a realistic approach for determining domain sizes < 20 nm.

In paper VII we continued the previous study and provided a detailed dynamic and structural study of crosslinker-triggered formation of nanodomains. We give evidence for existence of such structures in model plasma membranes at lipid compositions closely approaching the optically resolvable phase separation boundary. We revealed two types of domains: a) domains whose size becomes larger with increasing amount of added cholera toxin and to which CTxB binds tightly and b) domains formed in membranes with slightly increased amount of sphingomyelin (as compared to a) whose size does not change during titration by additional CTxB and to which CTxB binds less tightly. We explain the observed behaviour by ability of cholera toxin to compensate the lack of sphingomyelin in case a).

Finally, paper II investigates a) the controversial temperature behaviour of G_{M1} micelles and b) shows that the value of the diffusion coefficient of rhodamine 6G published in 1974 and used from that time for calibration of the focal volume was wrong. The aggregation numbers of G_{M1} micelles decrease from 30°C irreversibly with increasing temperature but remain unchanged ($N_{agg} = 168 \pm 4$ at 20°C) over a broad range of G_{M1} concentrations (0.76 – 156 μM). The aggregation numbers have been further used to calibrate the focal volume in FCS. Although the newly published rhodamine 6G diffusion coefficient provides a reasonable agreement between N_{agg}

obtained by energy transfer and FCS it is recommended to use the more precise calibration by means of known dye concentrations (preferably of 5-TAMRA).

5. ACKNOWLEDGEMENTS

Being supervised by Lennart Johansson and Martin Hof I have always considered a big advantage. Both of you gave me the scientific guidance I needed, were always optimistic and had good ideas how to solve problems we encountered. I also appreciate that you let me decided on my own, respected my ideas and enabled me to travel between Praha and Umeå whenever I thought it was necessary. I hope you have enjoyed the collaboration so much as I have.

Special thanks belong to you, Lennart, for welcoming us so friendly when we came to Umeå for the first time. I still remember the bag from ICA with fresh food and a Czech beer we got from you at the airport. I thank you for that you were so patient and started to speak Swedish with me. You were a good teacher in both fluorescence and Swedish.

I would like to thank to anybody who contributed to this work, especially to Jana for useful scientific discussions and for introducing me into the nanodomain problematic, Agnieszka for helping me with the pore project, Oleg for the computer help, Erik for the assistance with the G_{M1} project and improving English in several papers, to Radek for the help with generation of random positions on a bicelle and to Mirek Štěpánek, who guided me during the work on the solvent relaxation project.

I am obliged to our colleagues Ilya Mikhalyov, Natalya Gretskaya and Ivan Boldyrev from Moscow, who synthesized for us fluorescently labelled lipids that were not commercially available.

I am also very grateful to my wife Šárka for her support and love. We both know very well how difficult it was to combine our works here and in Umeå so that we could be the maximum time at the same place. It is cool that you became a specialist in damages of the Czech but also the Swedish concrete.

Many thanks belong also to Karel Miškovský from Umeå, who supplied Šárka with many interesting geological projects closely related to her work in Prague and enabled my wife to spend some time with me in Umeå.

6. REFERENCES

1. Przybylo, M.; Sýkora, J.; Humpolíčková, J.; Benda, A.; Zan, A.; Hof, M., Lipid diffusion in giant unilamellar vesicles is more than 2 times faster than in supported phospholipid bilayers under identical conditions. *Langmuir* **2006**, 22, (22), 9096-9099.
2. Sandström, M. C.; Johansson, E.; Edwards, K., Influence of preparation path on the formation of discs and threadlike micelles in DSPE-PEG(2000)/lipid systems. *Biophys. Chem.* **2008**, 132, (2-3), 97-103.
3. Lundquist, A.; Wessman, P.; Rennie, A. R.; Edwards, K., Melittin-Lipid interaction: A comparative study using liposomes, micelles and bilayer disks. *Biochim. Biophys. Acta-Biomembr.* **2008**, 1778, (10), 2210-2216.
4. Smith, A. K.; Freed, J. H., Determination of Tie-Line Fields for Coexisting Lipid Phases: An ESR Study. *J. Phys. Chem. B* **2009**, 113, (12), 3957-3971.
5. Hammond, A. T.; Heberle, F. A.; Baumgart, T.; Holowka, D.; Baird, B.; Feigenson, G. W., Crosslinking a lipid raft component triggers liquid ordered-liquid disordered phase separation in model plasma membranes. *Proc. Natl. Acad. Sci. U. S. A.* **2005**, 102, (18), 6320-6325.
6. Heberle, F. A.; Wu, J.; Goh, S. L.; Petruzielo, R. S.; Feigenson, G. W., Comparison of Three Ternary Lipid Bilayer Mixtures: FRET and ESR Reveal Nanodomains. *Biophys. J.* **99**, (10), 3309-3318.
7. Chiantia, S.; Ries, J.; Kahya, N.; Schwille, P., Combined AFM and two-focus SFCS study of raft-exhibiting model membranes. *ChemPhysChem* **2006**, 7, (11), 2409-2418.
8. Silvius, J. R.; Nabi, I. R., Fluorescence-quenching and resonance energy transfer studies of lipid microdomains in model and biological membranes (Review). *Mol. Membr. Biol.* **2006**, 23, (1), 5-16.
9. Jurkiewicz, P.; Sýkora, J.; Olzynska, A.; Humpolíčková, J.; Hof, M., Solvent relaxation in phospholipid bilayers: Principles and recent applications. *J. Fluoresc.* **2005**, 15, (6), 883-894.
10. Kalman, B.; Clarke, N.; Johansson, L. B.-Å., Dynamics of a New Fluorescent-probe, 2,5,8,11-tetra-tert-butylperylene in Solutions, Cubic Lyotropic Liquid-crystals and Model Membranes. *J. Phys. Chem.* **1989**, 93, (11), 4608-4615.
11. Lakowicz, J. R., *Principles of Fluorescence Spectroscopy*. Third ed.; Springer: Singapore, 2006.
12. Valeur, B., *Molecular Fluorescence Principles and Applications*. Wiley-VCH Verlag GmbH: Weinheim, 2001.
13. Förster, T., Zwischenmolekuläre Energiewanderung und Fluoreszenz. *Ann. Phys.-Berlin* **1948**, 2, (1-2), 55-75.
14. Isaksson, M.; Norlin, N.; Westlund, P. O.; Johansson, L. B.-Å., On the quantitative molecular analysis of electronic energy transfer within donor - acceptor pairs. *Phys. Chem. Chem. Phys.* **2007**, 9, (16), 1941-1951.
15. Baumann, J.; Fayer, M. D., Excitation Transfer in Disordered Two-dimensional and Anisotropic Systems- Effects of Spatial Geometry on Time-resolved Observables. *J. Chem. Phys.* **1986**, 85, (7), 4087-4107.
16. Johansson, L. B.-Å.; Engström, S.; Lindberg, M., Electronic Energy Transfer in Anisotropic Systems. 3. Monte-Carlo Simulations of Energy Migration in. *J. Chem. Phys.* **1992**, 96, (5), 3844-3856.
17. Engstrom, S.; Lindberg, M.; Johansson, L. B.-Å., Monte-Carlo Simulations of Electronic-Energy transfer in 3-dimensional Systems – A comparison with Analytical Theories. *J. Chem. Phys.* **1988**, 89, (1), 204-213.

18. Marushchak, D.; Grenklo, S.; Johansson, T.; Karlsson, R.; Johansson, L. B.-Å., Fluorescence depolarization studies of filamentous actin analyzed with a genetic algorithm. *Biophys. J.* **2007**, 93, (9), 3291-3299.
19. Jesenská, A.; Sýkora, J.; Olzynska, A.; Brezovský, J.; Zdráhal, Z.; Damborský, J.; Hof, M., Nanosecond Time-Dependent Stokes Shift at the Tunnel Mouth of Haloalkane Dehalogenases. *J. Am. Chem. Soc.* **2009**, 131, (2), 494-501.
20. Sýkora, J.; Jurkiewicz, P.; Epand, R. M.; Kraayenhof, R.; Langner, M.; Hof, M., Influence of the curvature on the water structure in the headgroup region of phospholipid bilayer studied by the solvent relaxation technique. *Chem. Phys. Lipids* **2005**, 135, (2), 213-221.
21. Fee, R. S.; Maroncelli, M., Estimating the time-zero spectrum in time-resolved emission measurements of solvation dynamics. *Chem. Phys.* **1994**, 183, (2-3), 235-247.
22. Macháň, R.; Hof, M., Recent Developments in Fluorescence Correlation Spectroscopy for Diffusion Measurements in Planar Lipid Membranes. *Int. J. Mol. Sci.* **11**, (2), 427-457.
23. Elson, E. L.; Magde, D., Fluorescence correlation spectroscopy. 1. Conceptual basis and theory. *Biopolymers* **1974**, 13, (1), 1-27.
24. Magde, D.; Elson, E. L.; Webb, W. W., Fluorescence correlation spectroscopy. 2. Experimental realization. *Biopolymers* **1974**, 13, (1), 29-61.
25. Karolin, J.; Johansson, L. B.-Å.; Strandberg, L.; Ny, T., Fluorescence and absorption spectroscopic properties of dipyrrometheneboron difluoride (BODIPY) derivatives in liquids, lipid membranes and proteins. *J. Am. Chem. Soc.* **1994**, 116, (17), 7801-7806.
26. Bergstrom, F.; Mikhalyov, I.; Hagglof, P.; Wortmann, R.; Ny, T.; Johansson, L. B. A., Dimers of dipyrrometheneboron difluoride (BODIPY) with light spectroscopic applications in chemistry and biology. *J. Am. Chem. Soc.* **2002**, 124, (2), 196-204.
27. Mikhalyov, I.; Gretskaya, N.; Bergström, F.; Johansson, L. B.-Å., Electronic ground and excited state properties of dipyrrometheneboron difluoride (BODIPY): Dimers with application to biosciences. *Phys. Chem. Chem. Phys.* **2002**, 4, (22), 5663-5670.
28. Balter, A.; Nowak, W.; Pawelkiewicz, W.; Kowalczyk, A., Some remarks on the interpretation of the spectral properties of prodan. *Chem. Phys. Lett.* **1988**, 143, (6), 565-570.
29. London, E., Investigation of membrane structure using fluorescence quenching by spin labels – A review of recent studies. *Mol. Cell. Biochem.* **1982**, 45, (3), 181-188.
30. Raghuraman, H.; Shrivastava, S.; Chattopadhyay, A., Monitoring the looping up of acyl chain labeled NBD lipids in membranes as a function of membrane phase state. *Biochim. Biophys. Acta-Biomembr.* **2007**, 1768, (5), 1258-1267.
31. Menger, F. M.; Keiper, J. S.; Caran, K. L., Depth-profiling with giant vesicle membranes. *J. Am. Chem. Soc.* **2002**, 124, (40), 11842-11843.
32. Sheynis, T.; Sýkora, J.; Benda, A.; Kolusheva, S.; Hof, M.; Jelínek, R., Bilayer localization of membrane-active peptides studied in biomimetic vesicles by visible and fluorescence spectroscopies. *Eur. J. Biochem.* **2003**, 270, (22), 4478-4487.
33. Chalpin, D. B.; Kleinfeld, A. M., Interaction of fluorescence quenchers with the normal 9-(anthroyloxy) fatty-acid membrane probes. *Biochimica Et Biophysica Acta* **1983**, 731, (3), 465-474.
34. Marsh, D., Membrane water-penetration profiles from spin labels. *Eur. Biophys. J. Biophys. Lett.* **2002**, 31, (7), 559-562.
35. Chattopadhyay, A.; London, E., Parallax method for direct measurement of membrane penetration depth utilizing fluorescence quenching by spin-labelled phospholipids. *Biochemistry* **1987**, 26, (1), 39-45.
36. Sýkora, J.; Slavíček, P.; Jungwirth, P.; Barucha, J.; Hof, M., Time-dependent stokes shifts of fluorescent dyes in the hydrophobic backbone region of a phospholipid bilayer:

- Combination of fluorescence spectroscopy and ab initio calculations. *J. Phys. Chem. B* **2007**, 111, (21), 5869-5877.
37. Villalain, J.; Prieto, M., Location and interaction of N-(9-anthroyloxy)-stearic acid probes incorporated in phosphatidylcholine vesicles. *Chem. Phys. Lipids* **1991**, 59, (1), 9-16.
 38. Seelig, A.; Seelig, J., Effect of a single cis double-bond on structure of a phospholipid bilayer. *Biochemistry* **1977**, 16, (1), 45-50.
 39. Luckey, M., *Membrane Structural Biology with Biochemical and Biophysical Foundations*. Cambridge University Press: New York, 2008.
 40. D.D.Lasic, *Liposomes from Physics to Applications*. Elsevier: Amsterdam, London, New York, Tokyo, 1995.
 41. Ludtke, S. J.; He, K.; Heller, W. T.; Harroun, T. A.; Yang, L.; Huang, H. W., Membrane pores induced by magainin. *Biochemistry* **1996**, 35, (43), 13723-13728.
 42. Yang, L.; Weiss, T. M.; Lehrer, R. I.; Huang, H. W., Crystallization of antimicrobial pores in membranes: Magainin and protegrin. *Biophys. J.* **2000**, 79, (4), 2002-2009.
 43. Matsuzaki, K.; Sugishita, K.; Ishibe, N.; Ueha, M.; Nakata, S.; Miyajima, K.; Epand, R. M., Relationship of membrane curvature to the formation of pores by magainin 2. *Biochemistry* **1998**, 37, (34), 11856-11863.
 44. Šachl, R.; Uchman, M.; Matějíček, P.; Procházka, K.; Štěpánek, M.; Špírková, M., Preparation and characterization of self-assembled nanoparticles formed by poly(ethylene oxide)-block-poly(epsilon-caprolactone) copolymers with long poly(epsilon-caprolactone) blocks in aqueous solutions. *Langmuir* **2007**, 23, (6), 3395-3400.
 45. Weber, G.; Farris, F. J., Synthesis and spectral properties of a hydrophobic fluorescent probe - 6-propionyl-2-(dimethylamino)naphthalene. *Biochemistry* **1979**, 18, (14), 3075-3078.
 46. Viard, M.; Gallay, J.; Vincent, M.; Meyer, O.; Robert, B.; Paternostre, M., Laurdan solvatochromism: Solvent dielectric relaxation and intramolecular excited-state reaction. *Biophys. J.* **1997**, 73, (4), 2221-2234.
 47. Parasassi, T.; Krasnowska, E. K.; Bagatolli, L.; Gratton, E., LAURDAN and PRODAN as polarity-sensitive fluorescent membrane probes. *J. Fluoresc.* **1998**, 8, (4), 365-373.
 48. Allen, C.; Maysinger, D.; Eisenberg, A., Nano-engineering block copolymer aggregates for drug delivery. *Colloid Surf. B-Biointerfaces* **1999**, 16, (1-4), 3-27.
 49. Teng, Y.; Morrison, M. E.; Munk, P.; Webber, S. E.; Procházka, K., Release kinetics studies of aromatic molecules into water from block polymer micelles. *Macromolecules* **1998**, 31, (11), 3578-3587.
 50. Wall, M. E.; Wani, M. C.; Cook, C. E.; Palmer, K. H.; McPhail, A. T.; Sim, G. A., Plant antitumor agents. I. Isolation and structure of Camptothecin a novel alkaloidal leukemia and tumour inhibitor from Camptotheca acuminata. *J. Am. Chem. Soc.* **1966**, 88, (16), 3888-3890.
 51. Govindac.Tr; Ravindra.Kr; Viswanat.N, Mappicine, a minor alkaloid from mappia-foetida miers. *J. Chem. Soc.-Perkin Trans. I* **1974**, (11), 1215-1217.
 52. Cegelski, L.; Pinkner, J. S.; Hammer, N. D.; Cusumano, C. K.; Hung, C. S.; Chorell, E.; Aberg, V.; Walker, J. N.; Seed, P. C.; Almqvist, F.; Chapman, M. R.; Hultgren, S. J., Small-molecule inhibitors target Escherichia coli amyloid biogenesis and biofilm formation. *Nat. Chem. Biol.* **2009**, 5, (12), 913-919.
 53. Pemberton, N.; Pinkner, J. S.; Jones, J. M.; Jakobsson, L.; Hultgren, S. J.; Almqvist, F., Functionalization of bicyclic 2-pyridones targeting piles biogenesis in uropathogenic Escherichia coli. *Tetrahedron Lett.* **2007**, 48, (26), 4543-4546.
 54. Šachl, R.; Mikhalyov, I.; Hof, M.; Johansson, L. B.-Å., A comparative study on ganglioside micelles using electronic energy transfer, fluorescence correlation spectroscopy and light scattering techniques. *Phys. Chem. Chem. Phys.* **2009**, 11, (21), 4335-4343.

55. Uhlík, F.; Limpouchová, Z.; Matějíček, P.; Procházka, K.; Tuzar, Z.; Webber, S. E., Nonradiative excitation energy transfer in hydrophobically modified amphiphilic block copolymer micelles. theoretical model and Monte Carlo simulations. *Macromolecules* **2002**, 35, (25), 9497-9505.
56. Almeida, P. F. F., Thermodynamics of lipid interactions in complex bilayers. *Biochim. Biophys. Acta-Biomembr.* **2009**, 1788, (1), 72-85.
57. Frazier, M. L.; Wright, J. R.; Pokorný, A.; Almeida, P. F. F., Investigation of domain formation in sphingomyelin/cholesterol/POPC mixtures by fluorescence resonance energy transfer and Monte Carlo simulations. *Biophys. J.* **2007**, 92, (7), 2422-2433.
58. Reigada, R.; Buceta, J.; Gomez, J.; Sagues, F.; Lindenberg, K., Phase separation in three-component lipid membranes: From Monte Carlo simulations to Ginzburg-Landau equations. *J. Chem. Phys.* **2008**, 128, (2), 10.
59. Garcia-Saez, A. J.; Chiantia, S.; Schwille, P., Effect of line tension on the lateral organization of lipid membranes. *J. Biol. Chem.* **2007**, 282, (46), 8.
60. Ursell, T. S.; Klug, W. S.; Phillips, R., Morphology and interaction between lipid domains. *Proc. Natl. Acad. Sci. U. S. A.* **2009**, 106, (32), 13301-13306.
61. Eggeling, C.; Ringemann, C.; Medda, R.; Schwarzmann, G.; Sandhoff, K.; Polyakova, S.; Belov, V. N.; Hein, B.; von Middendorff, C.; Schonle, A.; Hell, S. W., Direct observation of the nanoscale dynamics of membrane lipids in a living cell. *Nature* **2009**, 457, (7233), 1159-U121.
62. Lingwood, D.; Ries, J.; Schwille, P.; Simons, K., Plasma membranes are poised for activation of raft phase coalescence at physiological temperature. *Proc. Natl. Acad. Sci. U. S. A.* **2008**, 105, (29), 10005-10010.
63. Holowka, D.; Baird, B., Fc epsilon RI as a paradigm for a lipid raft-dependent receptor in hematopoietic cells. *Semin. Immunol.* **2001**, 13, (2), 99-105.
64. Benda, A.; Benes, M.; Marecek, V.; Lhotsky, A.; Hermens, W. T.; Hof, M., How to determine diffusion coefficients in planar phospholipid systems by confocal fluorescence correlation spectroscopy. *Langmuir* **2003**, 19, (10), 4120-4126.
65. Wawrzynieck, L.; Rigneault, H.; Marguet, D.; Lenne, P. F., Fluorescence correlation spectroscopy diffusion laws to probe the submicron cell membrane organization. *Biophys. J.* **2005**, 89, (6), 4029-4042.
66. Dietrich, C.; Volovyk, Z. N.; Levi, M.; Thompson, N. L.; Jacobson, K., Partitioning of Thy-1, GM1, and cross-linked phospholipid analogs into lipid rafts reconstituted in supported model membrane monolayers. *Proc. Natl. Acad. Sci. U. S. A.* **2001**, 98, (19), 10642-10647.
67. Marushchak, D.; Gretskaya, N.; Mikhalyov, I.; Johansson, L. B.-Å., Self-aggregation - an intrinsic property of G(M1) in lipid bilayers. *Mol. Membr. Biol.* **2007**, 24, (2), 102-112.
68. Cantu, L.; Corti, M.; delFavero, E.; Digirolamo, E.; Raudino, A., Thermal hysteresis phenomena in micellar solutions of gangliosides: Theory and experiments. *J. Phys. II* **1996**, 6, (7), 1067-1090.
69. Brocca, P.; Cantu, L.; Corti, M.; Del Favero, E.; Raudino, A., Collective phenomena in confined micellar systems of gangliosides. *Physica A* **2002**, 304, (1-2), 177-190.
70. Orthaber, D.; Glatter, O., Time and temperature dependent aggregation behaviour of the ganglioside GM1 in aqueous solution. *Chem. Phys. Lipids* **1998**, 92, (1), 53-62.
71. Webb, W. W., Fluorescence Correlation Spectroscopy Theory and Applications. In Rigler, R., Elson, E.S., Ed. Springer-Verlag: Berlin, 2001.
72. Muller, C. B.; Loman, A.; Pacheco, V.; Koberling, F.; Willbold, D.; Richtering, W.; Enderlein, J., Precise measurement of diffusion by multi-color dual-focus fluorescence correlation spectroscopy. *Epl* **2008**, 83, (4), 5.
73. Petrasek, Z.; Schwille, P., Precise measurement of diffusion coefficients using scanning fluorescence correlation spectroscopy. *Biophys. J.* **2008**, 94, (4), 1437-1448.